DEVELOPMENT OF A HANDHELD SCANNING TRANSDUCER PROBE FOR ULTRASOUND IMAGING

A Thesis

by

SHAKIR FAZLULLA MOHAMED

Submitted to the Office of Graduate and Professional Studies of
Texas A&M University
in partial fulfillment of the requirements for the degree of

MASTER OF SCIENCE

Chair of Committee,	Jun Zou
Committee Members,	Jun Kameoka
	Raffaella Righetti
	Gwo-Ping (Alex) Fang
Head of Department,	Begovic Miroslav M.

August 2015

Major Subject: Electrical Engineering

Copyright 2015 Shakir Fazlulla Mohamed

ABSTRACT

The scanning transducer technique is a simple and cost effective approach to achieve ultrasound imaging. By mechanically scanning a single-element transducer with a motor stage, the time-variant ultrasound field at an array of locations can be recorded for image reconstruction. When compared with the use of conventional transducer arrays, the scanning transducer approach requires much less data acquisition electronics. However, conventional x-y motor stages used for scanning the transducer are complex, bulky and slow. As a result, the scanning transducer technique for image acquisition has been mainly limited for lab use and is not suitable for handheld imaging applications.

The goal of this research is to achieve a new 2-axis scanning transducer probe for handheld ultrasound imaging operations, which is compact and light-weight. The approach is to develop and capitalize upon a miniaturized water-immersible 2-axis electromagnetic actuator to enable fast and agile scanning of a single-element transducer in a liquid filled probe case.

The design and fabrication of a water-immersible 2-axis electromagnetic actuator has been achieved and its mechanical scanning performance has been characterized and optimized with finite-element simulation. Preliminary pulse-echo imaging experiments were performed to verify its ultrasound imaging capability with scanning in B-scan mode in multiple directions. The scan system built can be dynamically reconfigured to either 1D- B-Scan or even 2D C-Scan formats for conventional 2D as well as 3D ultrasound imaging. In addition, integrated optical light delivery with optic fiber cables was also investigated to extend its capability for photoacoustic imaging.

ACKNOWLEDGEMENTS

I would like to thank first and foremost my advisor, Dr. Jun Zou for providing me with the opportunity to be part of his excellent research team and encouraging me with guidance and direction in every step of the way. It has been a great privilege to work alongside some of the smartest and helpful people that I have had the good fortune of knowing during the course of the year that I have worked on this research project.

I would also like to thank my committee members Dr. Jun Kameoka, Dr. Raffaella Righetti and Dr. Alex (Gwo-Ping) Fang for taking the time to review my thesis and providing their valuable feedback.

I am very grateful to all the other graduate students in the research group- Chih-Hsien Huang, Song Xu, He Hu (Henry), Cheng Fang ,Young Cho and Akhil Kumar for their inputs and assistance during the course of my research. Many of you took time out from your busy schedules to help me with my research and provided valuable inputs which have helped me enormously.

Many thanks are also due to Dr.Jun Kameoka and Dr.Arum Han along with their research teams for providing the use of their lab facilities.

Finally, I would like to acknowledge the support of my family and friends, without whom it would not have been possible to enjoy my time at Texas A&M as much as I have.

NOMENCLATURE

US	Ultra Sound
PA	Photo Acoustic
PAI	Photo Acoustic Imaging
PRF	Pulse Repetition Frequency
NdFeB	Neodymium, Iron and Boron ($Nd_2Fe_{14}B$)
ROI	Region of Interest

TABLE OF CONTENTS

Page

LIST OF FIGURES

Page

LIST OF TABLES

Page

1. INTRODUCTION

1.1 Ultrasound imaging

Ultrasound imaging has been used in medical diagnostic and industrial fault isolation applications for over fifty years and is one of the most popular imaging techniques in use. It is easy to use, does not emit ionizing radiation and is relatively inexpensive when compared to competing imaging techniques such as MRI (Magnetic Resonance Imaging) and X-ray. Ultrasound images provide a real time cross sectional view of the subject, which is an invaluable diagnostic tool especially in medicine [1].

A majority of ultrasound (US).imaging today is performed using what is known as the B-scan mode or Brightness scan mode ultrasound technique with pulse-echo ultrasound. This method involves transmitting short bursts of a few cycles of ultrasound using a US transducer (sound frequency generally in the range of 1-20MHz) into the target to be imaged at a pulse repetition frequency (PRF) of several thousands of pulses per second. Depending on the acoustic impedance of the target, the ultrasound waves penetrate to different depths and some are reflected back to the transducer. The US pulse return time determines the depth of the target and its intensity determines physical properties (such as density of tissue vs bone) The direction of ultrasound propagation along the beam line is generally called the axial direction, and the direction in the image plane perpendicular to axial is called the lateral direction [1]. The ultrasound transducer itself is made of a piezoelectric material which converts a voltage signal to a mechanical ultrasonic sound wave and vice versa.

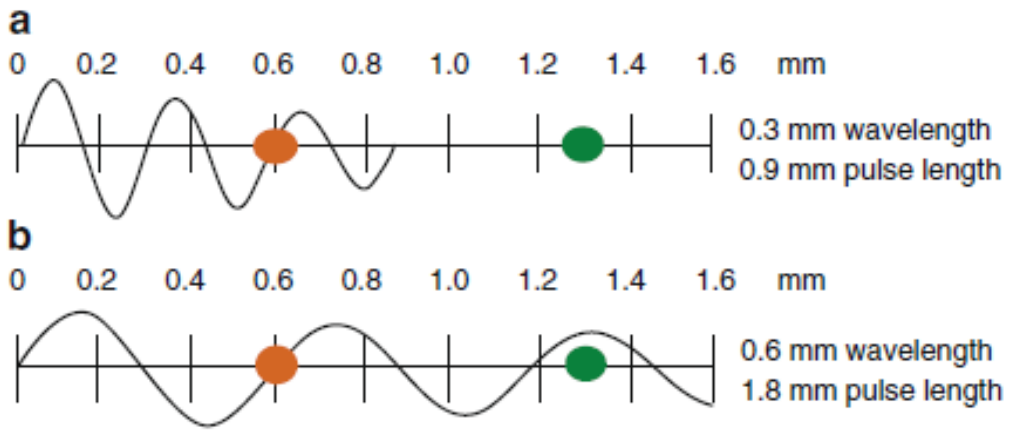

Figure 1.1. Attenuation and resulting penetration depth change of US waves with frequency.Higher frequency waves are attentuated more with depth than low frequency waves. Image reproduced from ref [1].

As the frequency of the US waves is increased, the image resolution increases, but penetration depth decreases. This is illustrated in figure 1.1 reproduced from [1].

US data can be represented in different ways depending on the method of acquisition. The most commonly used are A, B and C scan. A scan refers to Amplitude scan, where the US image is formed along a single line, and is a representation of the received US energy after the echo off the target as a function of time. Therefore, an A scan image is a plot of received US energy on the vertical axis and time on the horizontal axis. A B-scan representation replaces the horizontal axis with lateral distance and the vertical axis with depth (or time taken for echo return). The intensity of the signal received is generally represented by monochrome shades ranging from black (no obstruction to US signal such as in fluid) to white (where US pulse reflects off a hard surface like bone). C scan is the

same as B scan but along 2 dimensions and can be used to create a 3D image of the test subject. Figure 1.2 illustrates the different image representations, reproduced from ref [2].

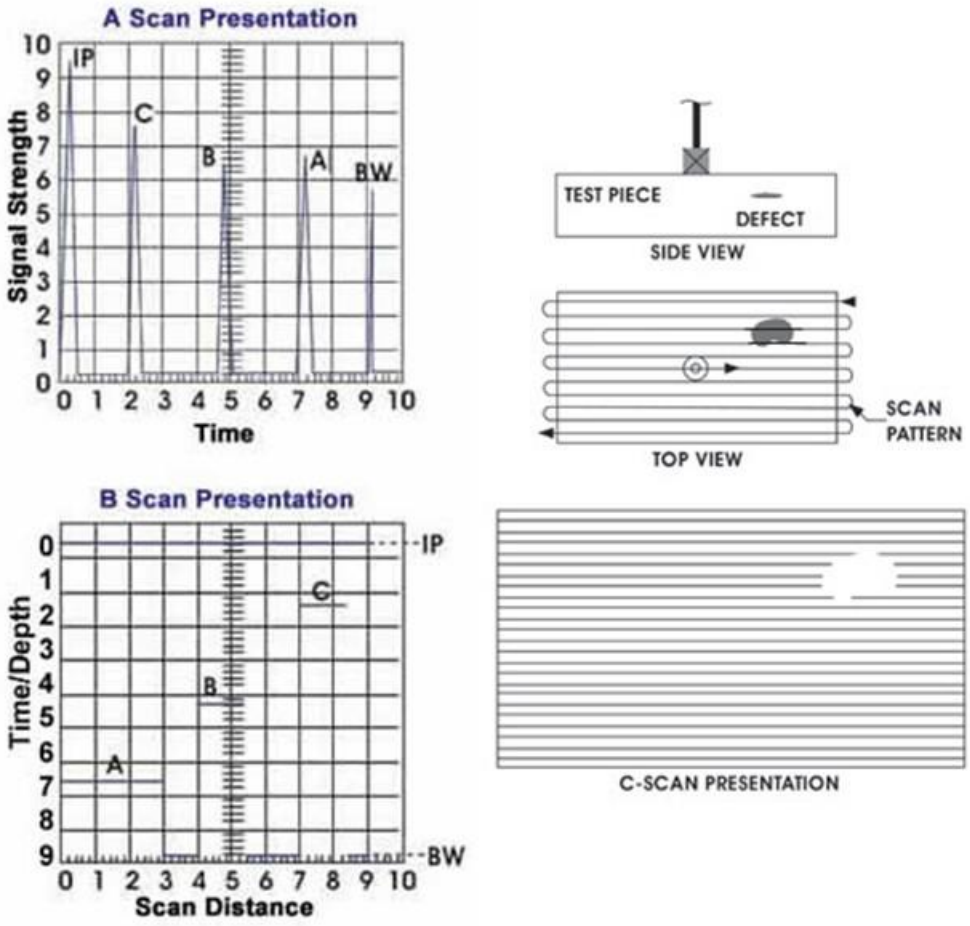

Figure 1.2. .A,B and C scan US imaging. IP is initial pulse, A,B C are imaging targets and BW is back wall. Images courtesy ref [2]

1.2 Scanning transducer technology

The lateral resolution of an ultrasound image depends upon the diameter of the unfocussed transducer. If a focused transducer is used, resolution can be improved, but the focus distance has a limited range. To improve lateral resolution of an unfocussed transducer, image processing algorithms such as SAFT (Synthetic aperture focusing technique) are used [3, 4].

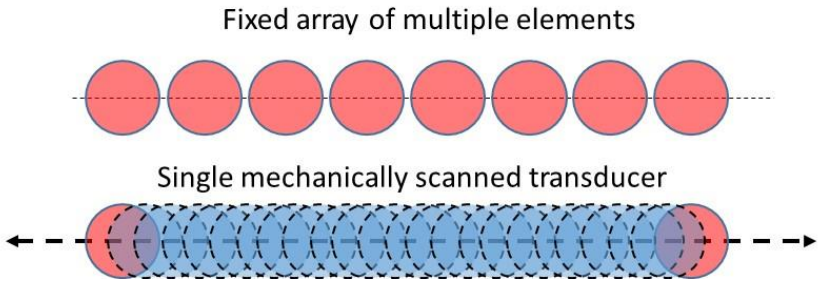

Figure 1.3. A multi element linear array Vs a virtual linear array formed by mechanically scanning a single transducer.

The most prevalent method used for US imaging is with a linear phased array of US transducers which generate B scan images and this technique gives a 2D cross sectional view of the target [5, 6]. The problem with using a linear array of multiple transducer elements is high cost because of the additional elements and associated signal routing and amplification circuitry and lower lateral resolution due to the finite space between each element. To gain lateral resolution, a single transducer can be mechanically scanned and a fast serial data transmission and acquisition system can be used to emulate

a linear or even 2D array of transducer elements. Such a virtual linear array is illustrated in figure 1.3 and compared to a traditional multi element linear array.

As can be seen in figure 1.3, the scanned transducer can be sampled at many positions in between the fixed arrays, leading to potentially much higher lateral image resolution. Vertical resolution depends on the frequency of the US transducer. For a given penetration depth, higher frequency US allows more number of pulses per unit time, which increases the number of available data points and hence resolution [1]. Additionally, a single transducer uses only one data line which greatly simplifies the supporting front end circuitry like amplifiers and not having to deal with routing signal lines efficiently to reduce cross talk, making a single element, high US frequency virtual array potentially a much more cost effective and superior solution when compared to a multi element array. This is especially true in the case of 3D imaging, where a dense 2 dimensional array of transducers is used [7, 8].

The limitation of current implementations of scanning virtual array transducer imaging systems is due to the fact that they are not very portable as seen in figure 1.4. These scanning transducer systems use either a single transducer or a one dimensional array of transducers in a benchtop setup with x,y,z stepping motors to scan over a target area [9, 10].

Some systems use probe positioning systems that need to track the precise location of a conventional linear US element array probe as it is scanned over a region of interest by hand for 3D imaging [11-13]. The research presented in this thesis focuses on developing a cost effective and compact, water-immersible, single-transducer mechanical

scanning system capable of linear B-scan style scanning in multiple planes as well as a 2 dimensional circular or spiral scanning pattern.

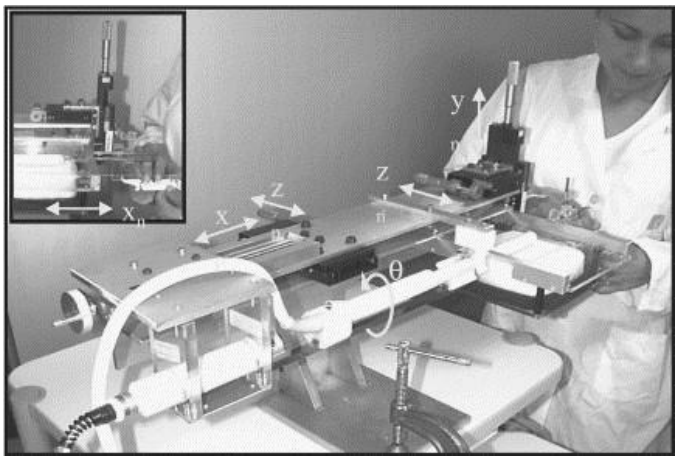

Figure 1.4. A scanning transducer system which uses an X-Y stage to mecahnically scan the transducer. Image repoduced from ref [13].

.

2. SCANNING PROBE DESIGN AND OPTIMIZATION

2.1 Scanning mechanism

2.1.1 Previous work

Figure 2.1 shows the general overview of an existing system that scans a single element US transducer in a 2 dimensional circular pattern for 3D imaging.

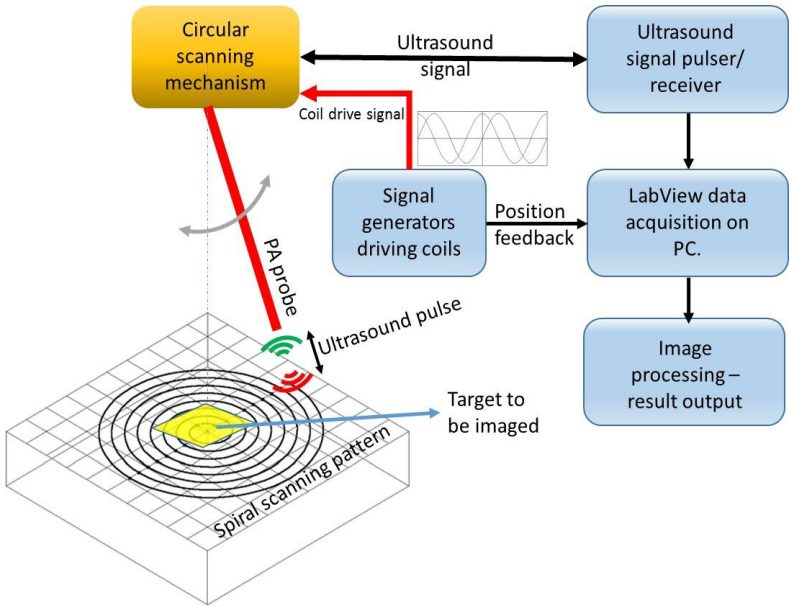

Figure 2.1. Overview of existing US imaging system in the lab. A spiral scanning pattern is traced by mechanically scanned probe. A PC controls the data acquisition and performs image reconstruction.

A bench top setup exists currently in the lab which consists of a cylindrical magnet attached to the ultrasound transducer coaxial cable, which is acted upon by force generated from coils arranged along the x and y axes as seen in figure 2.2. One end if the cable is

secured and kept at a suitable height. By feeding opposing coils a 180 degree phase shifted sinusoidal current, a push-pull effect is achieved, causing a deviation in the cable along that axis. By giving a 90 degree phase shift on the perpendicular axis, it is possible to scan the cable and the attached magnet in a circular pattern. The spiral shape is achieved by gradually varying the voltage of the coils. It can be seen that there are numerous parameters that can be changed that will affect the scanning angle of the single element US transducer.

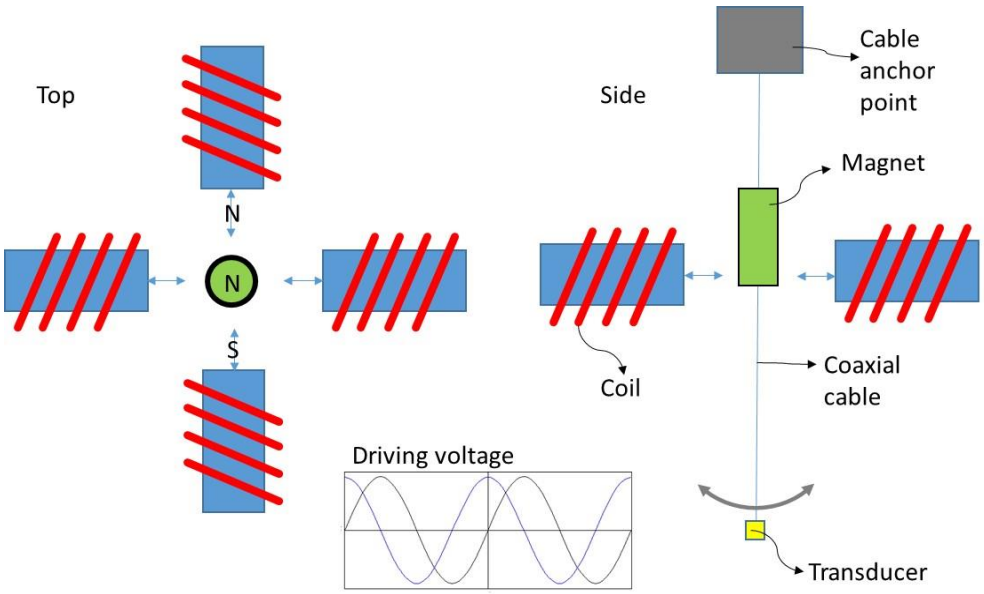

Figure 2.2. Existing 3D imaging bench setup in the lab. 4 sets of coils drive a magnet attached to the coax cable of the US transducer in X and Y directions enabling a circular scan pattern with 90 degree phase difference in driving currents.

2.1.2 Design of scanning mechanism

The angle by which the cable deflects depends upon the force acting on it as well as the stiffness of the cable. The force generated on a magnetic material separated by an air gap from a coil depends upon the number of turns, its core material and the current passing through it and is given by equation 2.1 [14]:

$$\boldsymbol{F = \frac{{F_m}^2 \mu_0 A}{2g^2}} \qquad \textbf{Equation 2.1}$$

$$\boldsymbol{F_m = N \times I} \qquad \textbf{Equation 2.2}$$

F_m is the magneto motive force, N=number of turns, I=current, μ= magnetic permeability, A =area of coil and g= air gap.

The stiffness k in turn is determined by the length of the cable between the magnet and the anchor point, given by equation 2.3 and 2.4 as [15]:

$$\boldsymbol{k = \frac{3EI}{L^3}} \qquad \textbf{Equation 2.3}$$

$$\boldsymbol{I = \frac{1}{12} m(3r^2 + L^2)} \qquad \textbf{Equation 2.4}$$

The restoring force F provided by this cable is then given by equation 2.5 as [15]:

$$\boldsymbol{F = k \times x} \qquad \textbf{Equation 2.5}$$

Where E= Elastic modulus of material, I = moment of inertia and L=length, r= radius, m=mass and x is the lateral displacement.

The design process involves selecting an appropriate combination of all these parameters that will result in a spiral scanning diameter of at least 30mm. To help with this decision making process, hand calculations along with software simulations for both the mechanical and electromagnetic properties were performed. Approximating the mechanical stiffness of a coaxial cable without appropriate equipment is extremely difficult and no characterization data exists from which to roughly estimate its value. Since one of the future goals of this research was to build a scanning transducer imaging system with light delivery capability for PA imaging in addition to US pulse-echo imaging, as a starting point, it was assumed that the coils will have to deflect six 400μm optic fiber cables along with the coaxial cable for the US transducer. Mechanical simulations in Solidworks were carried out assuming a silicon cantilever is being bent rather than a copper coaxial cable, since the coaxial cables stiffness is going to be negligible compared to the stiffens of the optic fiber cables. Additionally, to make the entire system more compact, it was decided that the driving coils be placed vertically rather than horizontally as shown in figure 2.2 previously. To transfer the force to the cable, we now need to fabricate a structure that will hold the magnets at a right angle to the cable. The entire concept is illustrated in figure 2.3.

By varying different lengths x and y and *l*, it is possible to design the entire system so that the transducer can be scanned over a circle of 30mm diameter. The entire length of the magnet holder arm was arbitrarily chosen to be 35mm which gives a value of 17.5mm for x. Assuming a vertical deviation of 10mm for the magnet holder arm x, it is straightforward to determine that the length y of the coaxial cable will need to be

approximately 15*17.5/10 = 26.25 mm. Table 2.1 shows the calculated lengths y for various applied vertical deviations of the x arm of figure 2.3.

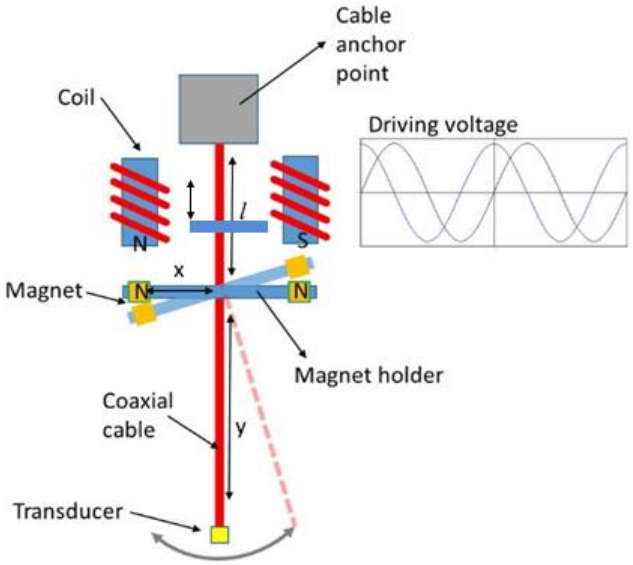

Figure 2.3. . Conceptual illustration of the proposed scanning mechanism. A 'magnet holder' allows bending force to be transferred to the cable from coils aranged vertically as shown. The principal of operation remains the same as the previous setup shown in figure 2.2.

x (mm)	y (mm)
1	262.50
2	131.25
3	87.50
4	65.63
5	52.50
6	43.75
7	37.50
8	32.81
9	29.17
10	26.25

Table 2.1. Calculated arm length y for given deflections x to maintain a 15mm deflection of the transducer at the end of the y arm.

From table 2.1, it can be seen that a reasonable physical design can be obtained for a wide variety of magnet arm deflections.

2.2 Design simulations and analysis

Figure 2.4 shows the result of a Solidworks mechanical bending simulation on a 30mm long silicon cable acted upon by a force of 1 Newton on one of the ends of the magnet holder arm, which resulted in a vertical deflection of a little over 9mm. The cable diameter was chosen to be ~2mm. (Section 5 describes in detail the reasoning for choosing this dimension).

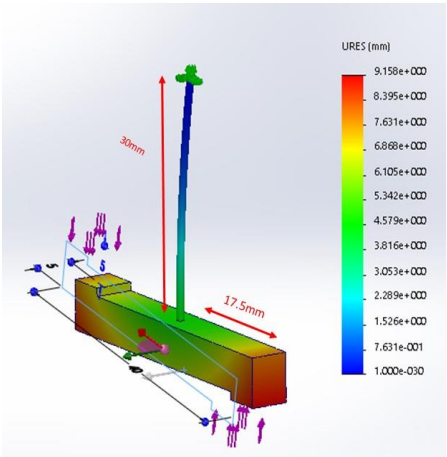

Figure 2.4. Solidworks simulation of a 30mm long silicon cable acted upon by a force of 1 Newton on one of the ends of the magnet holder arm resulted in a vertical deflection of 9.15mm. The entire span of the magnet holder arm was arbitralily chosen to be 35mm to ensure the whole system remains compact. See section 5 for more detail on why diameter of rod was chosen to be 2mm.

From the datasheet of the magnet used (KJ Magnetics part number D22-N52) [16], the pull force between 2 magnets is known to be around 1 Newton at a distance of 1.54mm from the magnet. The graph of pull force vs distance is shown in figure 2.5

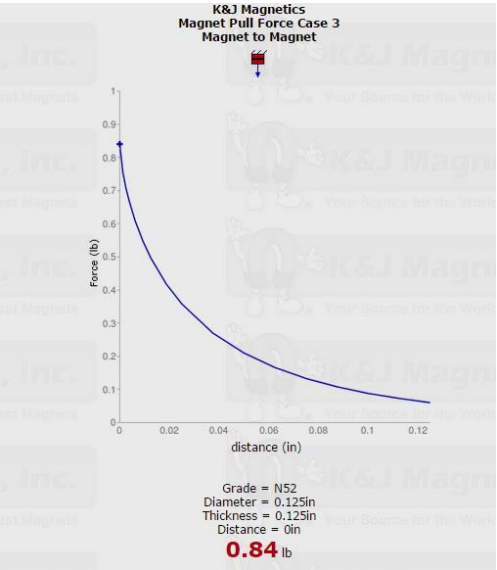

Figure 2.5. Magnet pull force vs distance. At around .06in from the magnet, it generates a pull force of 0.22 lb, which equates to about 1.5mm and 1N respectively. Image courtesy: KJ magnetics.

It is in the best interest of the design to maximize the possible pull force on the coaxial cable so that we have adequate margins to work with. The coils that are used in this setup are inductors sold by Digikey (part number M10176-ND) and have an inductance of 0.5 H , rated at 30mA and a DC resistance of 730 Ω. This was the largest inductor available in the catalog and was chosen because it has the largest number of turns. It is known that the inductance of a coil can be calculated with the formula [17]:

$$L = \frac{\mu N^2 A}{l}$$ **Equation 2.6**

Where μ is the magnetic permeability, N= number of turns, A= area of the coil and l is the length of the coil.

N(# turns)	R (m)	*l (m)*	w (m)	L(H)
5443	0.005715	0.016764	0.006251004	0.5

Table 2.2. Calculating number of turns of he coil using equation 2.7- Wheeler's formula modified for a ferrite core.

Back calculating given L= 0.5 Henry, $\mu = 4\pi \times 10^{-7} \times 640$ H/m for ferrite core [20], $A = \pi \times 0.008^2$ sq.m and l = 0.0223 m gives N=263 turns.

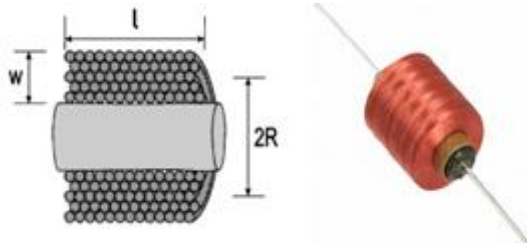

Figure 2.6. Illustrating the terms in Wheeler's formula. Image courtesy : http://coil32.net/theory/faq.html

Equation 2.6 holds true for a single layer solenoid. For a multilayer coil, we have Wheeler's formula which empirically determines the coil inductance for an air core solenoid as [18, 19]:

$$L = \frac{\mu_o N^2 R^2}{2\pi(6R+9l+10w)} \qquad \textbf{Equation 2.7}$$

As illustrated in figure 2.6, N= number of turns, R=Average radius of coil, *l*= length of coil, w= width of coil winding and μ_o is the magnetic permeability of air. In this application, we will have a multiplication factor of 640 to the permeability which is the relative permeability of the ferrite core [20]. The result of this calculation using equation 2.7 is shown in table 2.2

From equation 2.1, it is possible to calculate the theoretical magnetic force generated by this coil. Substituting the values from table 2.2 and assuming the gap g = 1mm and using the average radius R = 0.005 m, we get:

$$F = \frac{(5433\ turns \times 30\ mA)^2 \times 4\pi \times 10^{-7}\ \frac{H}{m} \times \pi \times .005^2\ sq.m}{2\times(1\ mm)^2} = 1.7\ N \qquad \textbf{Equation 2.8}$$

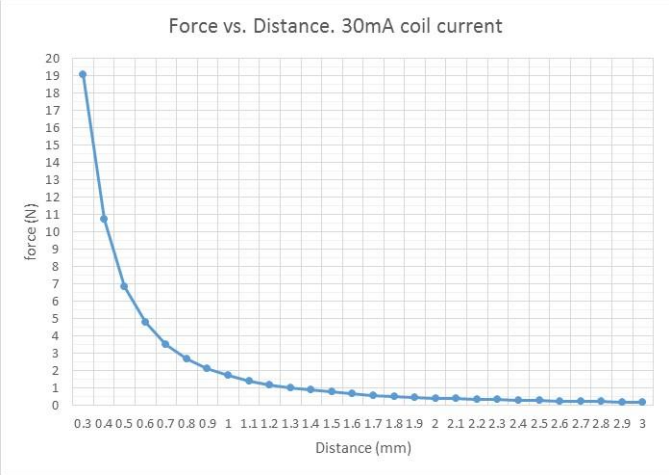

Figure 2.7. Force Vs distance for a ferromagnetic material with parameters taken from table 2.2 calculated using equation 2.8.

This is the approximate force experienced by a ferromagnetic material separated from the coil by 1mm in air. Figure 2.7 shows the variation of the force experienced by a ferromagnetic material for a range of distances from the coil. The scanning mechanism will use permanent magnets which will alter the force from the calculations in equation 2.8 and figure 2.7. The goal of this design process is to achieve approximately 1N of force to ensure that there is adequate deflection in the cable assembly which was obtained from the Solidworks simulation of figure 2.4. Calculating the force generated in this situation is more complicated and requires numerical computation and therefore cannot be easily approximated by hand calculations. Finite element analysis was carried out using the FEMM software tool and the resulting force generated on an NdFeB- N52 grade magnet by the coil was simulated. Figure 2.8 shows the simulation setup. The simulation depth was chosen to be 16mm- the thickness of the coil [21].

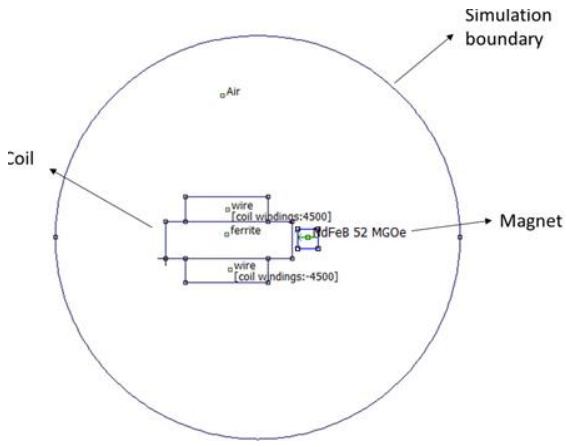

Figure 2.8. FEMM simulation setup. Magnet is separated from coil by 1mm. Initial simulations were run on a cylindrical magnet of 3.175mm diameter and height as per dimensions in datasheet of coil [21]. To increase the force generated, an additional magnet was used which is shown in simulation results in fig 2.11.

To ensure that the simulation represented the actual coil as closely as possible, it was initially simulated alone without any magnet and the DC resistance as well as the inductance was measured and matched with the values in the datasheet. The number of turns and the wire diameter was changed by trial and error until the inductance was close to 0.5 H and DC resistance was ~700 Ω.

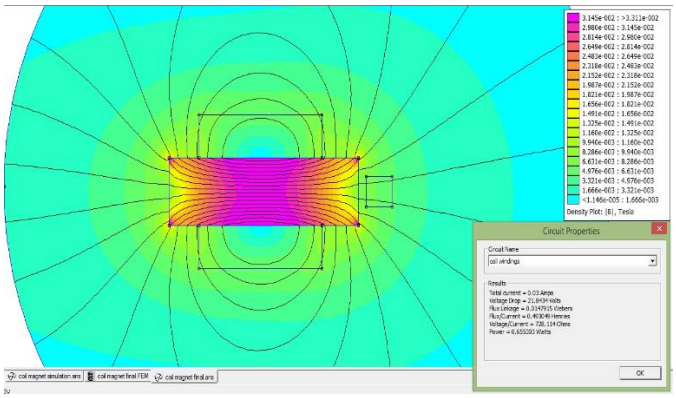

Figure 2.9. FEMM magnetic simulation and measurement of inductance and DC resistance. Inductance measured= 0.493 H, DC R= 728 Ω, Current though coil = 30mA (max rating of coil as per datasheet[21]) Number of turns = 4500.

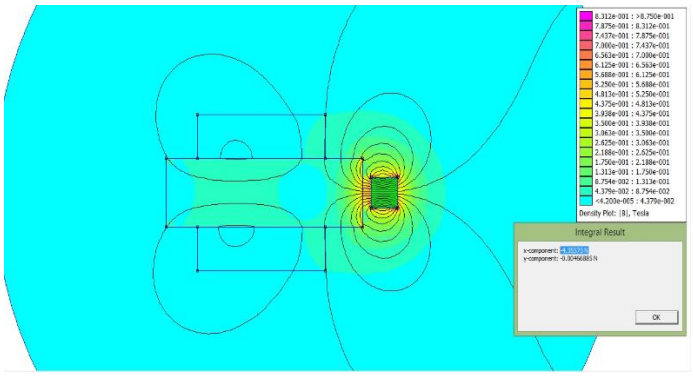

Figure 2.10. Force simulations on an NdFeB magnet cylindrical disk of length and diameter of 3.17mm seperated from the coil by 1mm. Current in the coil = 30mA.

The simulation results and measured values of the coil alone are shown in figure 2.9. The parameters measured were: Inductance = 0.493 H, DC R= 728 Ω which are close to the values of the actual coil being used. The current though the coil was set to 30mA (max rating of coil as per datasheet [21]) and the number of turns was found to be 4500 by running simulations by trial and error. The computed number of turns in table 2.2 is 5433 turns, which is reasonably close to the simulation value that produced the desired inductance of 0.5H. Now that the inductance and DC resistance of the coil match the actual coil datasheet, the NdFeB magnet was added to the simulation. The magnet shown in figure 2.10 is a cylindrical disk of diameter and height of 3.175mm (as per datasheet [16]). Three simulations were run to determine the actual force experienced by the magnet from the current in the coil. The first simulation was run with zero current in the coil, the second and third with +30 and -30 mA respectively. Since the core material is ferromagnetic, the permanent magnet separated from it by a distance experiences a pulling force towards the core. As both arms of the magnet holder will experience this force in the neutral position, the additional force generated by the magnetic field produced by the current carrying coil is what is responsible for bending the cable assembly. Table 2.3 shows force calculations done with a 3.17mm cylindrical NdFeB magnet. To calculate the actual force that will result in the bending of the cable, the force obtained with the simulation with zero current in the coil is subtracted with the force obtained with current flowing in the coil. Changing the direction of current flow- from +30mA to – 30mA results in a corresponding change in the direction of the force. Additionally, simulations were run assuming a larger square magnet attached to this cylindrical magnet to increase the

generated force, shown in figure 2.11. From the simulations carried out here, it is clear that this combination of coil and magnets should produce around 1N of peak force in each arm which will be adequate to bend the cable assembly

Small magnet			
Simulation Force (N)	current (A)	distance (mm)	Actual Force (N)
-4.90	0.00	1.00	
-4.36	0.03	1.00	0.55
-5.45	-0.03	1.00	-0.55
Large magnet			
Simulation Force (N)	current (A)	distance (mm)	Actual Force (N)
-7.98	0.00	1.00	
-6.92	0.03	1.00	1.07
-9.05	-0.03	1.00	-1.07

Table 2.3. Force calculation for a small 3.17mm cylindrical magnet resulting in a 0.5N force for each direction of current flow in the coil and an additional square magnet (6mm square by 1mm thick)- indicated as "large magnet" in table , to increase the pulling force to 1N.

2.3 Design optimization

The simulations and calculations so far have assumed that the magnet assembly is free to move only along one axis- the axis of the coil. However in practice, this is not going to be true as the cable will experience torsion forces even with a small misalignment of the magnet and the center of the coil causing it to twist and greatly reducing the desired

deflection amplitude as well as accuracy in the desired direction. This is illustrated in figure 2.12

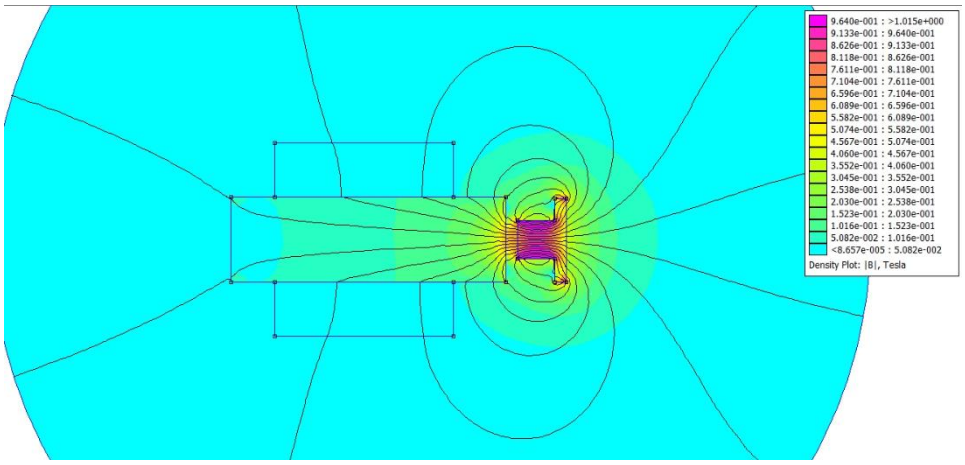

Figure 2.11. Simulation from larger square magnet attached to the earlier smaller magnet to increase force to ~1N.

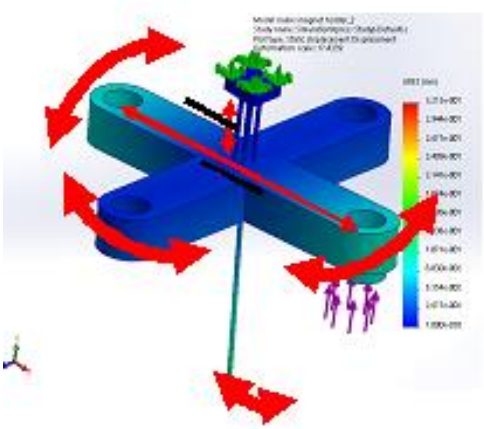

Figure 2.12. Torsion of the entire assembly will cause undesirable and uncontrolled deflection of the cable asembly.

To overcome the effect of torsion a gimbal mechanism was created to guide the cable

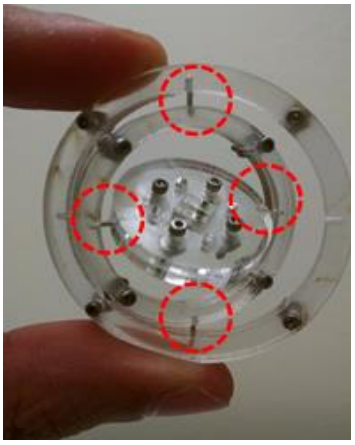

Figure 2.13. Gimbal mechanism laser cut in acryllic used to isolate the x and y axis forces and prevent torsion. The first prototype had pivots (circled in red) which were stiff metal wires cut to size by hand. Repeated cycling of the pivots caused excessive wear in the acryllic joints and caused loss of alignment.

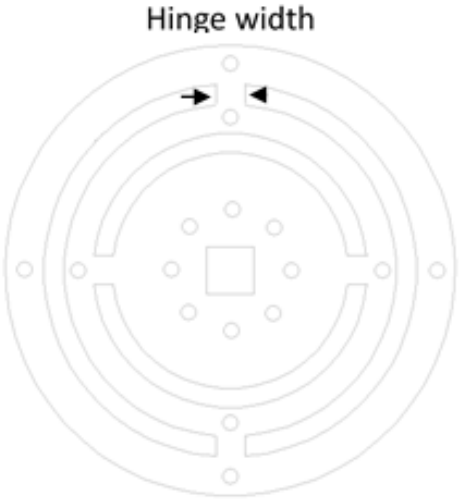

Figure 2.14. CAD drawing of laser cut pattern on a 300 micron plastic sheet to form hinges with built in stiffness. Stacking multiple sheets on top of eahc other increases the hinge stiffness, emulating the torsion of a rectangular cantilever beam.

assembly along the x and y directions independently and isolate the two forces from each other. The gimbal mechanism is shown in figure 2.13.

Despite using the gimbal mechanism, after several experiments, it was determined that the coaxial cable provides uneven stiffness along the x and y axes, causing an unstable scanning pattern. Also, anchoring the cable so that it presents an equal stiffness in every direction as well as ensuring that the cable returns to the exact same zero position at the end of each scan cycle proved to be extremely difficult with this setup.

To overcome these issues, the pivots in the gimbal mechanism had to be fabricated such that they provided additional stiffness and can withstand many cycles of movement. This was achieved by cutting sheets of 300 micron plastic patterned on a laser cutting station as shown in figure 2.14. This laser cut plastic sheet is sandwiched between the acrylic frame shown in figure 2.13 and held together with screws. Mechanical simulations were re run on this structure to determine the dimensions of the hinge that would result in around 5mm deflection at the magnet arm with 1N of applied force. Figure 2.15 shows the SolidWorks simulation result along both axes. The hinge width used was 1.5mm, with a height of 0.5mm (roughly 2 sheets stacked on top of each other). To increase the linearity of the deflection, it is important to limit the vertical deflection of the magnet arm as much as possible since the magnetic force follows an inverse square relationship with distance (figure 2.7). This means increasing the magnet arm-to-transducer length (length y in figure 2.3) to compensate for the reduced magnet arm deflection.

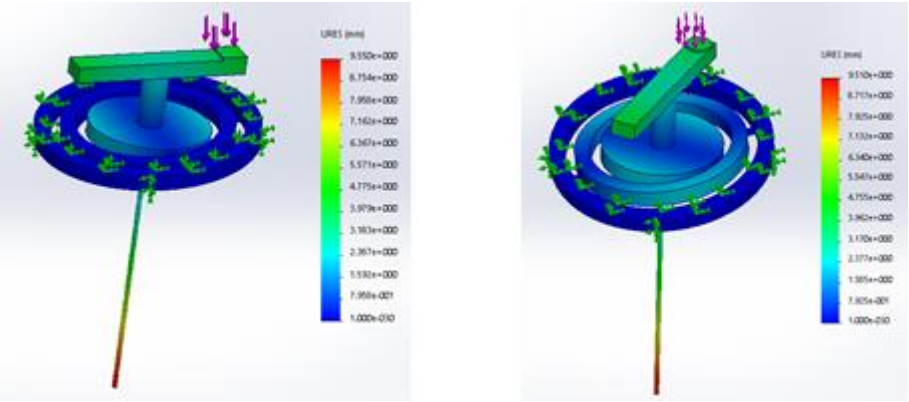

Figure 2.15. Solidworks simulation for the gimbal mechanism with the sandwiched plastic sheet hinge. Force applied =1N, Arm length from center= 17.5mm (35mm total). Hinge width= 1.5mm, hinge thickness = 0.5mm resulting in a 5mm deflection of the magnet arm (green in figure).

3. SCANNING PROBE CONSTRUCTION AND CHARACTERIZATION

3.1 Scanning probe construction

Figure 3.1 shows the design that was used to build the final prototype. It incorporates the gimbal mechanism presented in section 2.3 into the vertically mounted coils explained earlier. The gimbal mechanism has thin plastic sheets or around 300 micron thickness (red in figure 3.1) in between the rigid acrylic frame (grey) which are responsible for providing an even restoring force in all directions of deflection and also to ensure that the probe returns to the same zero position after each scan.. The transducer coaxial cable (white) is pushed through a rigid hollow tube (blue) and the transducer tip (yellow, extreme right). The rigid tube was incorporated to ensure there is no additional bending of the coaxial cable as it scans a circular or longitudinal pattern, which will prevent nonlinearity of the scan pattern with respect to applied voltage to the coils. The tube itself is attached to the gimbal mechanism using silicone glue. The “cable support” section (grey, extreme left) anchors the coaxial cable at one end to the extreme left. Its length can be varied to change the effective stiffness of the cable seen by the magnet actuation mechanism. The cable is held in the support structure with silicone glue. The entire structure is made by laser cut acrylic of 2mm thickness (figure 3.2) and held together with 1mm diameter steel screws and bolts. The hollow plastic tubing (shown in blue in figure 3.1) can also be used to hold optical fibers in place for light delivery for photoacoustic imaging. This is explored in detail in section 5. Scanning performance and mechanical characterization of the scan system is discussed in section 3.2

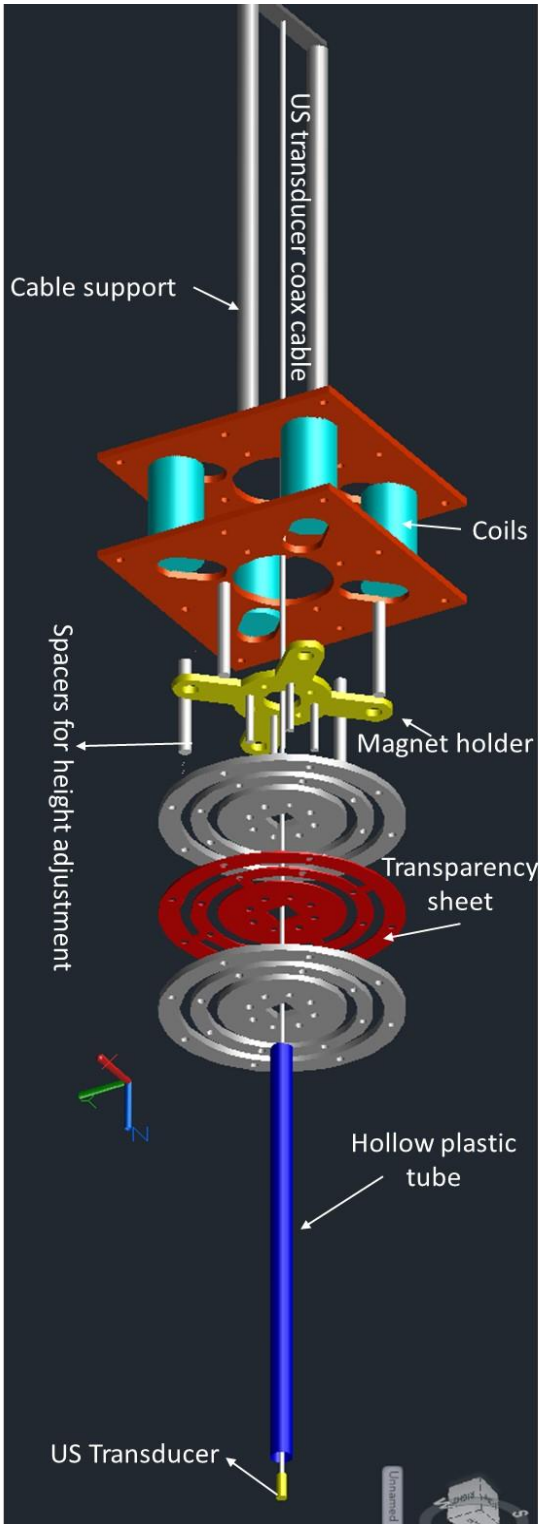

Figure 3.1. Design used to build the final prototype.

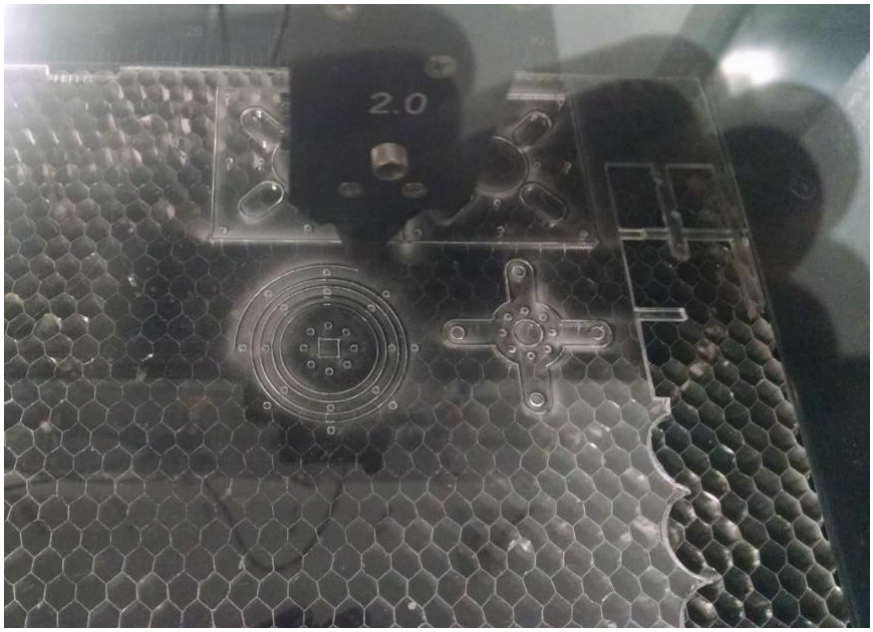

Figure 3.2. Laser cuting the components used in the construction of the probe.

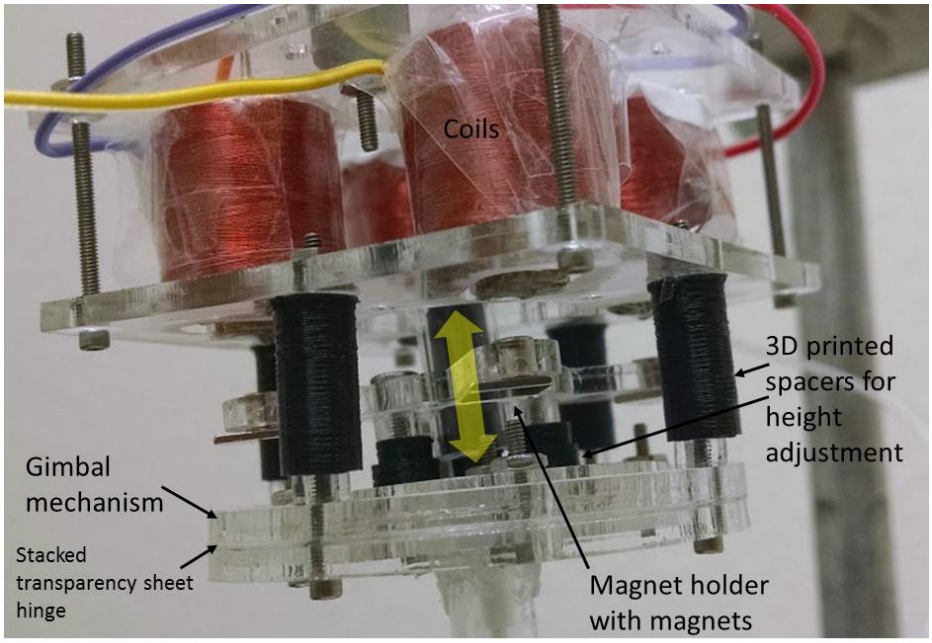

Figure 3.3. Close up view of the scanning mechanism showing the gimbal, magnets and drive coils along with the spacers used to adjust the distance between the magnets and the coils. Yellow arrow is direction of magent motion.

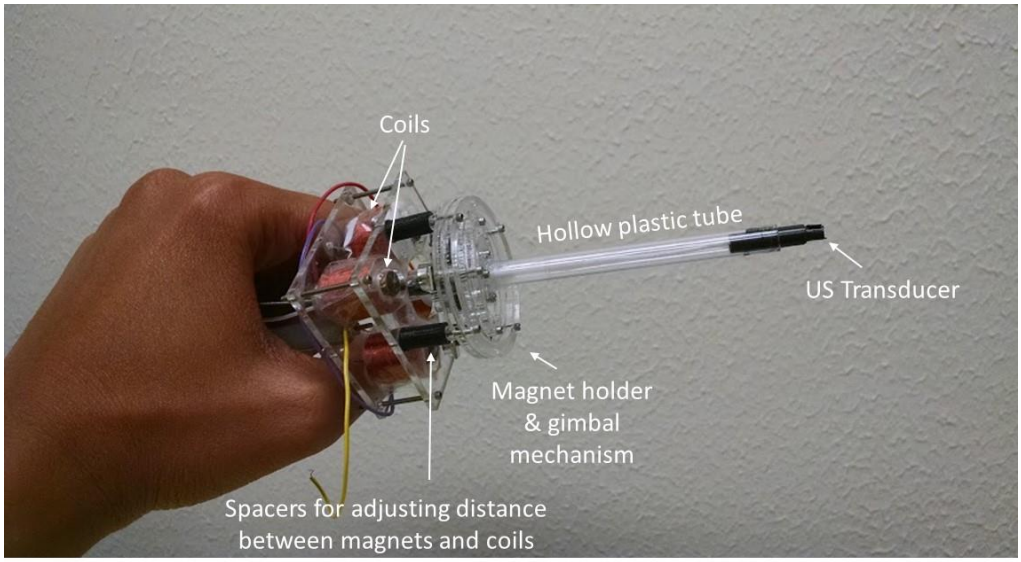

Figure 3.4. Fully assembled US scanning probe mechanism.

3.2 Scanning angle characterization

To determine the actual performance of the design, we look at the deviation of the scanning probe end with respect to the applied voltage. Since the DC resistance of these coils is around 750 Ω, the signal generators alone are sufficient to provide the driving current since they are rated to drive a 50Ω load up to 10V pk-pk. No current amplifier was used to drive the coils. The setup used to characterize the scanning pattern and deviation with applied voltage is shown in figure 3.5. The applied sinusoidal voltage was varied from 1V to 10 V pk-pk in steps of 1V and the resulting horizontal deviation of the laser spot was measured. The resulting deflection angle was calculated using simple trigonometry tangent function since the vertical length of the cable is known. The maximum deflection occurs at the mechanical resonant frequency of the entire setup. The

resonant frequency of this setup was measured manually by keeping the driving voltage to the maximum 10V from the signal generator, varying the frequency and visually observing the resulting deflection traced by the laser spot

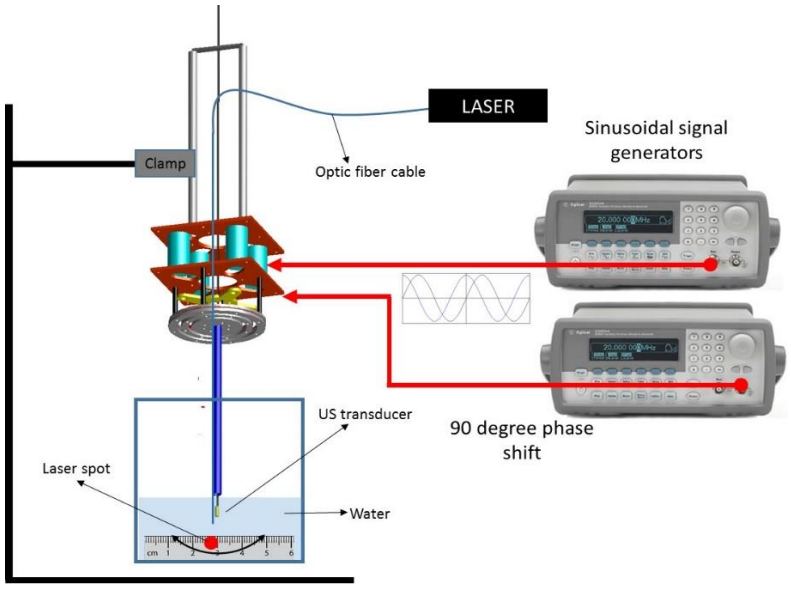

Figure 3.5. The scanning angle is characterized by visually observing the laser spot traced on a scale placed inside the water container in thich the probe is being scanned. By simultaneously applying a phase shifted voltage to the perpendicular coils, it is possible to scan the probe in a circular pattern or create a linear B-Scan with different angles.

A vertical cable length of 90mm was chosen for this prototype and the resulting resonant frequency was found to be 7.7Hz. Table 3.1 shows the deviation recorded for each voltage applied to the coils. A maximum deflection of ~ 28mm was achieved. The equivalent angle at the gimbal is calculated and plotted in figure 3.6. The angular deviation is found to be fairly linear with applied voltage, but there is still some nonlinearity due to

the uneven stiffness of the coaxial cable feeding the ultrasound transducer. A camera was placed under the scanning probe and photographs taken in long exposure mode (>1 sec) to generate trails from the CW laser coupled to the thin optic fiber shown in figure 3.5.

Volts	x (mm)		y (mm)	
	+	-	+	-
10	14	14	14	14
9	13	13	13	13
8	11	11	12	12
7	10	10	10	10
6	7	7	7	7
5	6	6	6	6
4	5	5	4	5
3	4	4	3	3
2	2	2	2	1
1	1	1	0.5	0.5

Table 3.1. Characterization data of probe end deflection with respect to voltage applied to coils. Voltage is peak to peak.

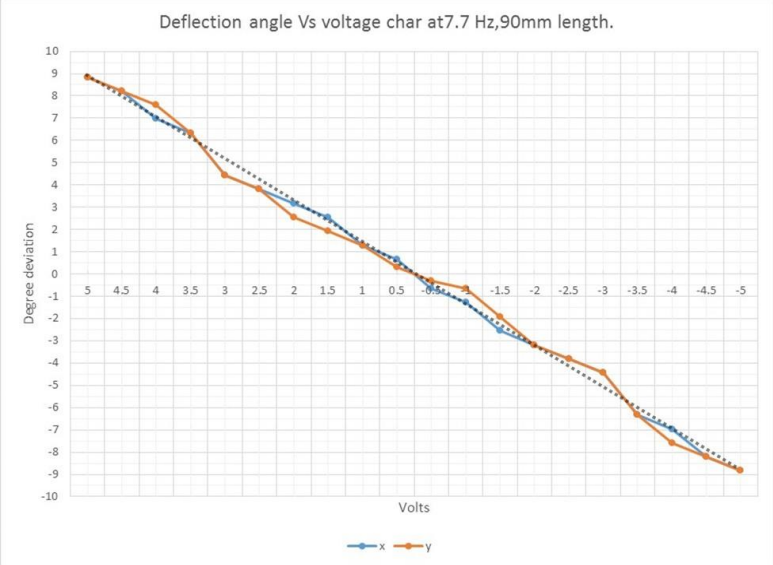

Figure 3.6. Calculated angular deflection with applied voltage. Maximum angle of deflection is 8.8 degrees. Dashed line represents ideal characterestics.

Figure 3.7 and 3.8 show the scan pattern shape produced in linear B-scan mode and circular scanning which was achieved by varying the phase difference between the 2 sets of coils.

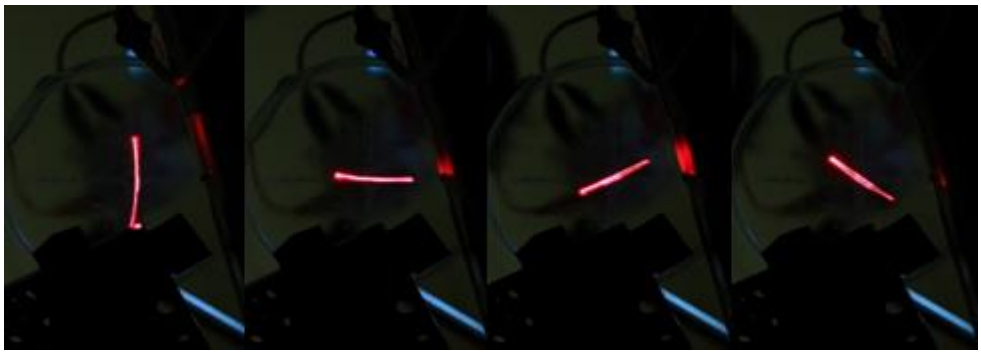

Figure 3.7. Scanning pattern in B-Scan mode.

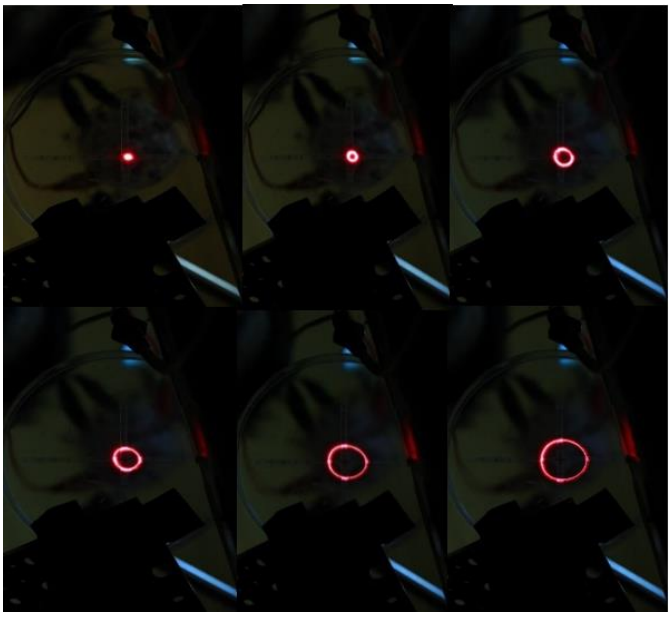

Figure 3.8. Circular scanning pattern with varying scan diameters.

It is possible to produce scan pattern ranging from a straight line to an ellipse to circular by changing the phase and amplitude of the driving coils.

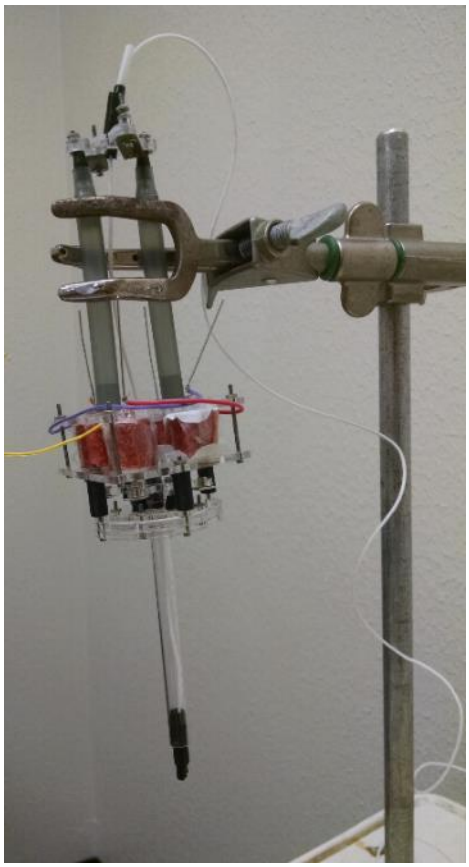

Figure 3.9. Part of the setup used for generating characterization data.

A photograph of the setup is shown in figure 3.9. A longer and more flexible thin plastic straw of 200 mm length was used as the hollow plastic tube in the setup to reduce the deflection angle of the magnets in an attempt to further improve linearity and scan range. While the lower mass and longer length resulted in a larger 32mm deflection (vs

28mm for this setup), the deflection was not very linear with applied voltage as shown in figure 3.10. This behavior was due to the bending of the tube itself as it was scanned. If the tube length is increased to achieve larger scan, it is necessary to maintain its stiffness. Using a carbon fiber tube is one alternative, but was not explored in this research.

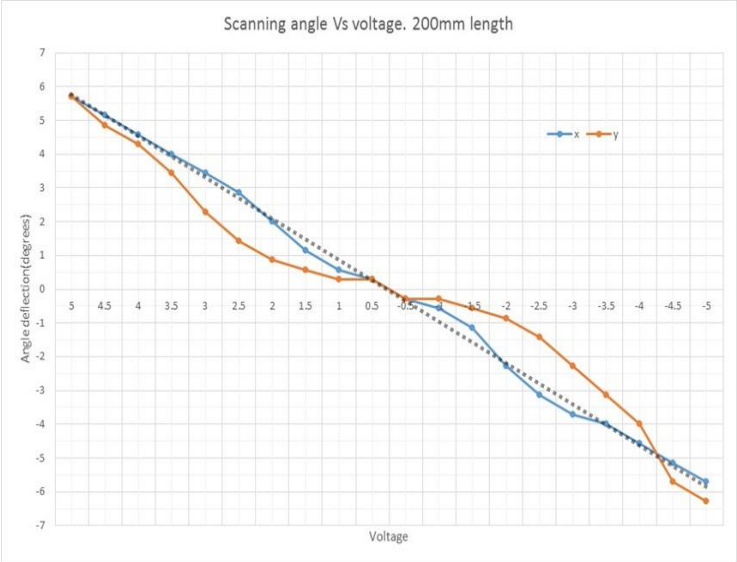

Figure 3.10. Deflection angle characterization data for 200mm long arm. Results are not as linear compared to stiffer arm setup shown previously in figure 3.6.

Although the scan patterns in figure 3.8 look more or less circular, there is slight distortion in the pattern which can be seen more easily in the stacked image shown in figure 3.11. The 3D image reconstruction algorithms used to create the final 3D image after scanning the transducer needs the probe to scan very precise circular patterns each varying by less than 0.5mm in diameter. This is needed because the image reconstruction algorithm is open loop and determines the position of the transducer by looking at the

voltage amplitude and phase of the driving coils.

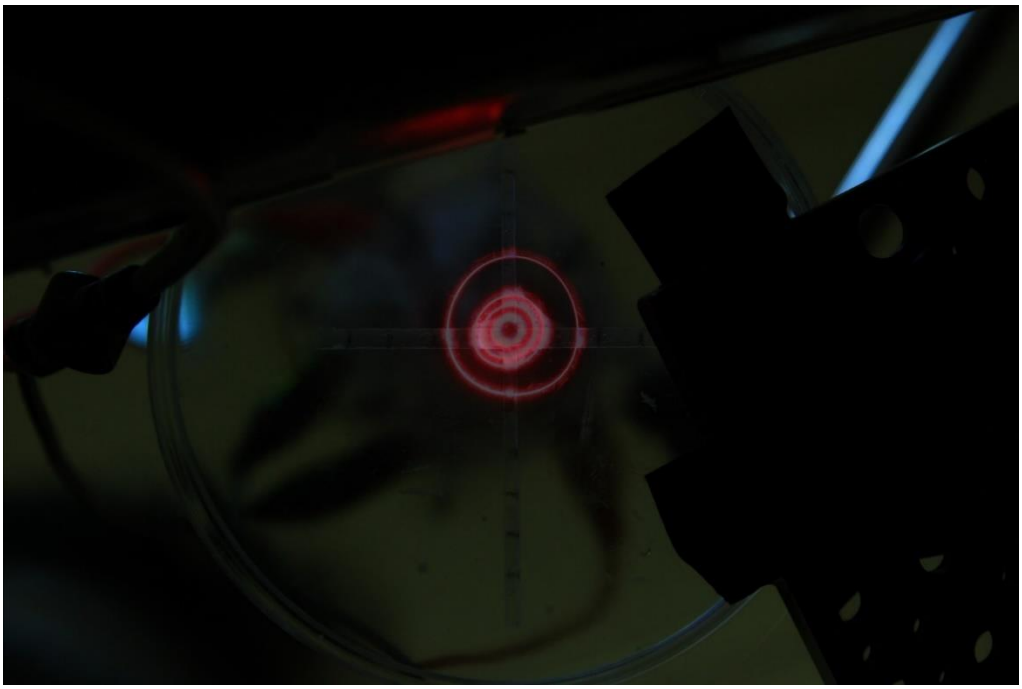

Figure 3.11. Stacked compiosite image showing distortion of circular pattern as diameter increases.

The reason for this distortion is the uneven stiffness presented by the coaxial cable attached to the transducer. Since it is a commercially available device, it is not possible to change the coaxial cable and this is a limiting factor in the scanning probe's performance. Maintaining a circular path also required different adjustments of the voltage and phase of the x and y axis coils for each diameter. Figure 3.12 shows the voltage changes on the coils as well as the corresponding phase difference that had to be introduced to maintain the circular shape of the scan pattern. Since this system is completely open loop, any

mechanical disturbance or even a slight shift in the cable would cause the circular scan pattern to get distorted and would require recalibration.

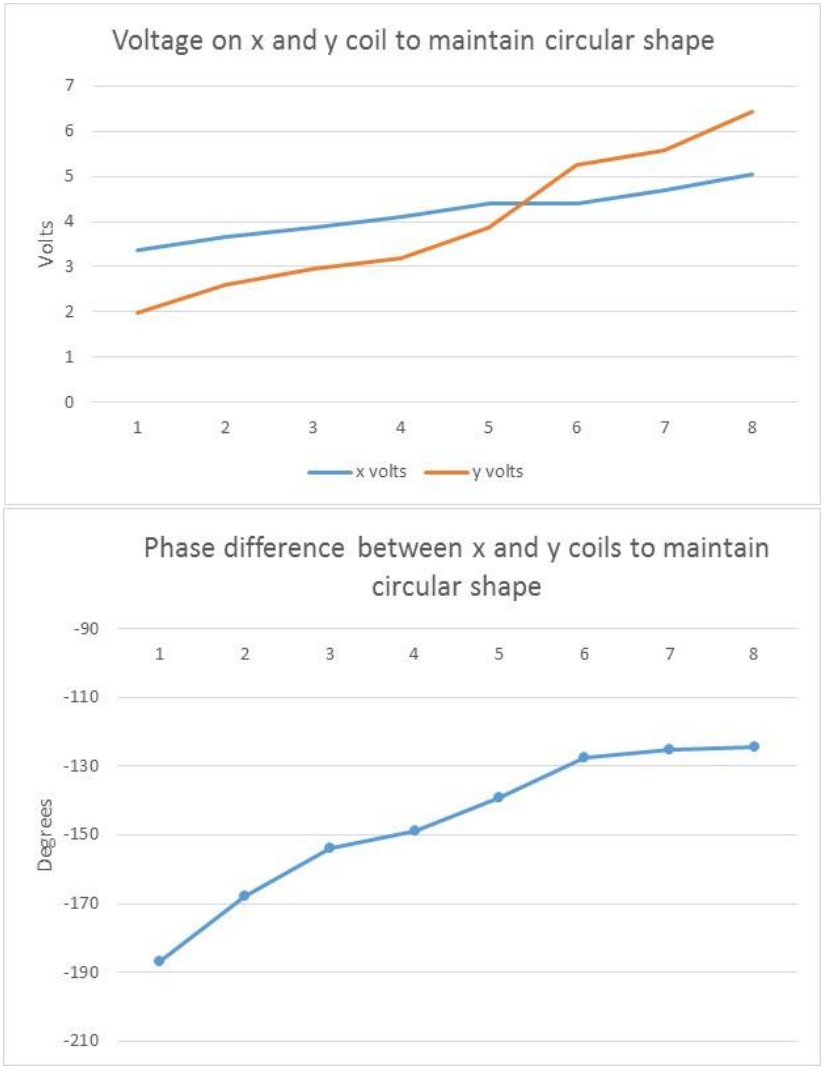

Figure 3.12. Voltage and phase changes needed to maintain a circular scan pattern as the diameter is increased. X axis represnets an increasing circle diameter traced out by the probe.

4. ULTRASOUND IMAGING RESULTS

4.1 Imaging setup and data acquisition

To test the imaging capability of the setup, a 2D B-scan was performed on a 0.9 mm pencil lead as a target.

Figure 4.1. Target used for B-scan imaging. The acryllic holder has porvision to hold several pencil leads of 0.9mm diameter and varying heights and seperations.

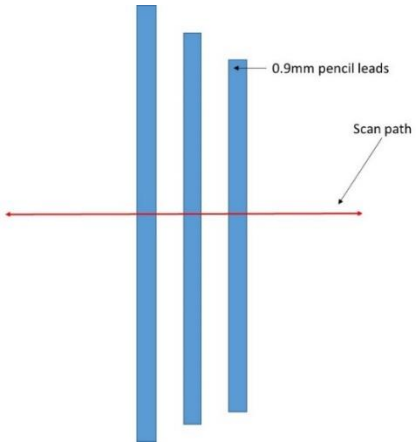

Figure 4.2. Conceptual diagram showing arrangement of pencil lead targets and scan path. The leads were seperated both along the x axis and the depth Z axis.

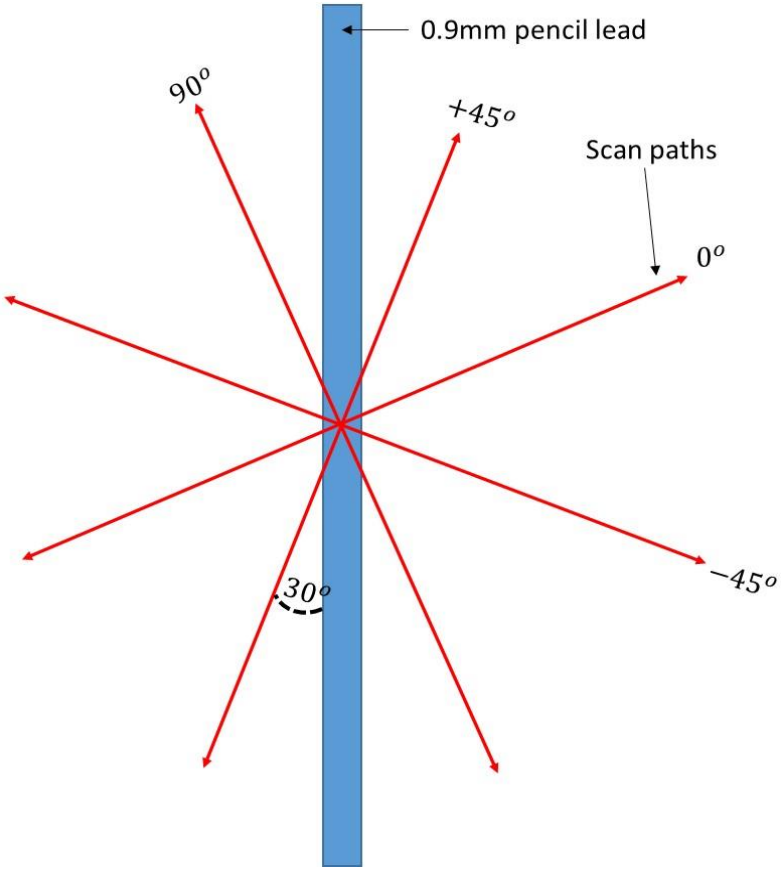

Figure 4.3. Multiple B-scan paths for a single pencil lead target.The 45 and 90 degree paths will result in a larger cross section than the 0 anf 90 degree paths due to the finite width of the pencil lead.

A picture of the target is shown in figure 4.1. One, two and three pencil leads were imaged together in three separate runs to test for resolution. The test setup is shown in figure 4.2. Four different B-scans were also performed on the pencil lead target as shown conceptually in figure 4.3 to demonstrate the programmability of the scan direction of the probe. The phase of the driving coils was changed so that the probe scanned the path shown in the red arrows for each combination of phase angle between the 2 sets of coils. The pencil lead target was offset from the 45 degree scan path by 30 degrees as shown in

figure 4.3 to ensure that only the cross section of the pencil lead was imaged and that no scan path would coincide with the entire length of the pencil lead to ensure consistency in the imaging results. Multiple B-scans at smaller angles covering the entire target can be potentially stacked together to build a 3D image of the target. The change in scan angle is achieved by varying the phase of the driving coils as shown in figure 4.4. A zero and ninety degree scan is performed by simply driving either of the 2 perpendicular pairs of coils.

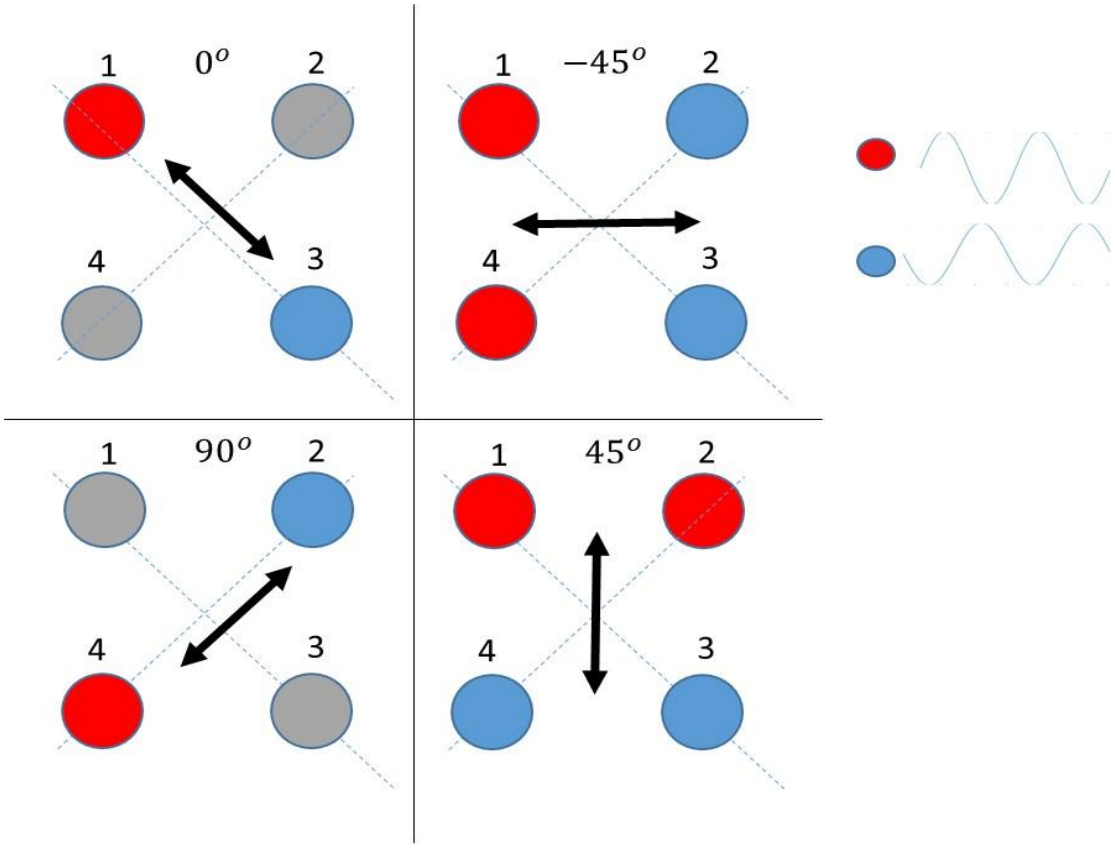

Figure 4.4. Driving current of each individual coil for desired scan direction. Red and Blue are ON with a 180 degree phase shift, Grey is off.

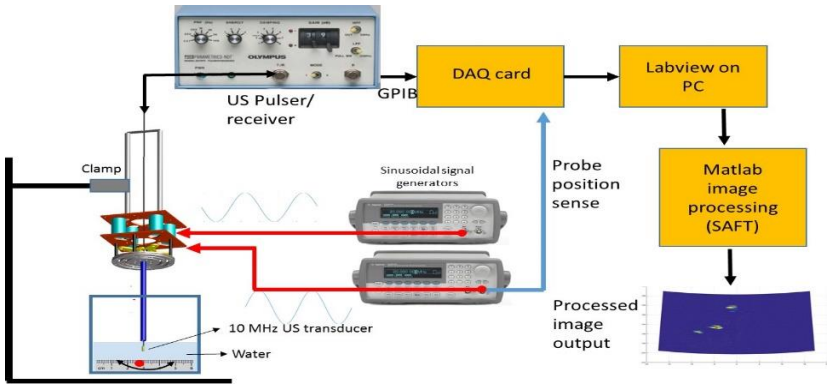

Figure 4.5. Overall US data acquisition setup.

To achieve +/- 45 degree scans, a phase difference of 180 degrees is given to the adjacent sets of coils. This is illustrated in figure 4.4 to show how the individual coils are driven to achieve the desired scan direction. The overall setup for the data acquisition is shown in figure 4.5. A US pulser/ receiver (5072PR, Olympus) is used to generate and receive the echo ultrasound pulses. The transducer used is rated at 10 MHz and a pulse repetition rate of 2 KHz was used. The pulser/receiver is connected to a data acquisition card (DAQ) connected to a PC running Labview via a GPIB bus. The Labview code determines the position of the US scanning probe by sampling the sinusoidal drive signal of one of the pairs of the coils shown schematically in figure 4.5. Since this is an open loop system, the assumption is that the driving sinusoidal signal is an accurate representation of how the position of the scanned transducer head changes with time, which is necessary for successful image reconstruction. The image is further processed by a Matlab script that runs an SAFT (Synthetic aperture focusing technique) algorithm that helps in improving contrast and resolution of the image. SAFT is discussed in more detail in section 4.2

4.2 Image reconstruction using SAFT

Synthetic aperture focusing technique (SAFT) is a method of image enhancement used in US imaging which improves lateral resolution by processing several successive measurements. It works by mimicking acoustic lenses used for focusing US beams at a point by using software algorithms rather than physical hardware. The main benefits of SAFT are improvement of lateral resolution and improvement of contrast by reducing backscattering effects [22]. The most common implementation of SAFT uses a delay and sum (DAS) of the time domain signal and is most commonly used in phased arrays. In this implementation, the US probe is a sort of a virtual phased array since it is mechanically scanned along a particular axis to be imaged, however, the principle is still the same as a traditional phased array. Figure 4.6 reproduced from ref [22] shows the 2D geometry of an array of US transducers imaging a target in the region of interest (ROI)

The US transducer is scanned along the y axis and transmits the US pulses along the x axis as shown in figure 4.6 For the US beam to be focused in the ROI, the SAFT algorithm works by performing a sum of the time shifted signals of the echo it receives. The time delays between each received signal from the observation point can be expressed in equation 4.1 as:[22]

$$\frac{2}{c}\left(\sqrt{x'^2 + (y' - u_n)^2} - x'\right) \qquad \textbf{Equation 4.1}$$

for n = 0, 1, ..., L – 1, where L is the number of element positions, r_n is the straight line distance from the element, u_n is the position of the transducer.

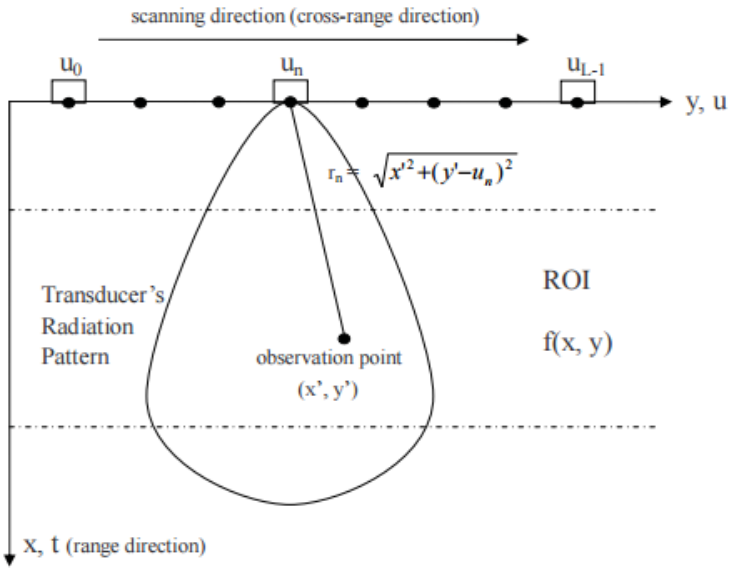

Figure 4.6. 2D cross section view of a linear phased array imaging a target in the region of interest (ROI). Image reproduced from ref[22].

By summing all the echo signals received by the transducer at all different scan positions, and correcting for the time delay using equation 4.1, the SAFT algorithm enhances contrast since the backscatter component of the received signal gets cancelled out since it is random in nature compared to the actual signal from the target, which gets further enhanced by the summation process.

4.3 US imaging results

Figure 4.7 shows the results obtained by a single B-scan for the target configured as shown in figure 4.2

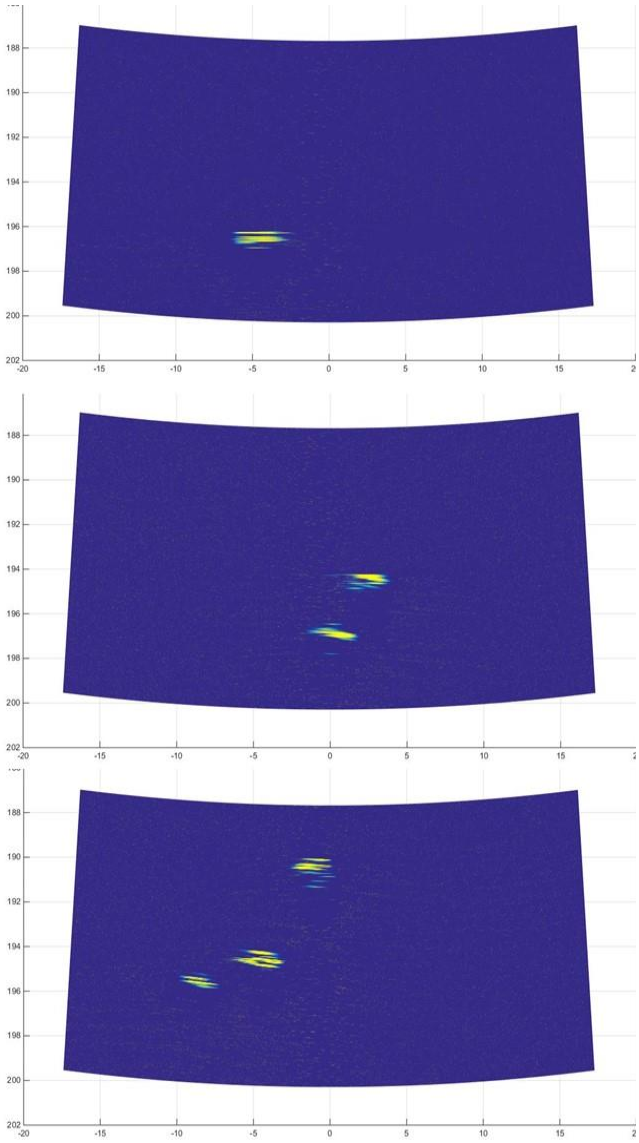

Figure 4.7. 2D B-scan image results of a 0.9 mm pencil lead target for 1, 2 and 3 leads. Note different depths (vertical axis) and similar thickness of each lead (horizontal axis) All dimensions are in mm.

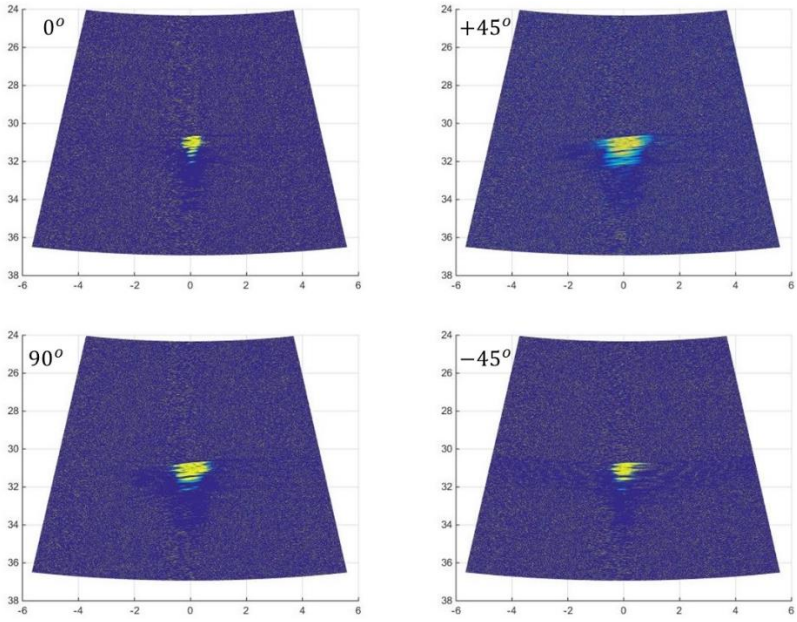

Figure 4.8. B-Scan imaging results for different scan angles shown in figure 4.4. X axis is target width and Y axis is depth in mm.

Separate B-scans were performed with one, two and three 0.9mm diameter pencil leads as targets. The vertical axis represents depth and the horizontal axis the width. It can be seen in figure 4.7 that the second and third images have the pencil leads at different depths. Figure 4.8 shows the multiple scan results of a single pencil lead in the configuration of figure 4.3. From the imaging results, it can be seen that +45 and 90 degree scans are slightly wider than the other two scans. This is because at these scan angles, as seen from figure 4.3, the apparent cross section is larger than at 0 and -45 degrees. By stacking several such B-scans at a smaller separation angle, it is possible to capture the entire cross section of a target and ultimately generate a 3D image. Imaging was not possible with the circular scan pattern due to instability discussed in the previous section.

5. INTEGRATION OF OPTICAL LIGHT DELIVERY

5.1 Integrating optical fibers for light delivery

Photoacoustic Imaging (PAI) makes use of the photoacoustic effect to create high contrast optical-absorption images of biological samples at a penetration depth up to several centimeters [23, 24].

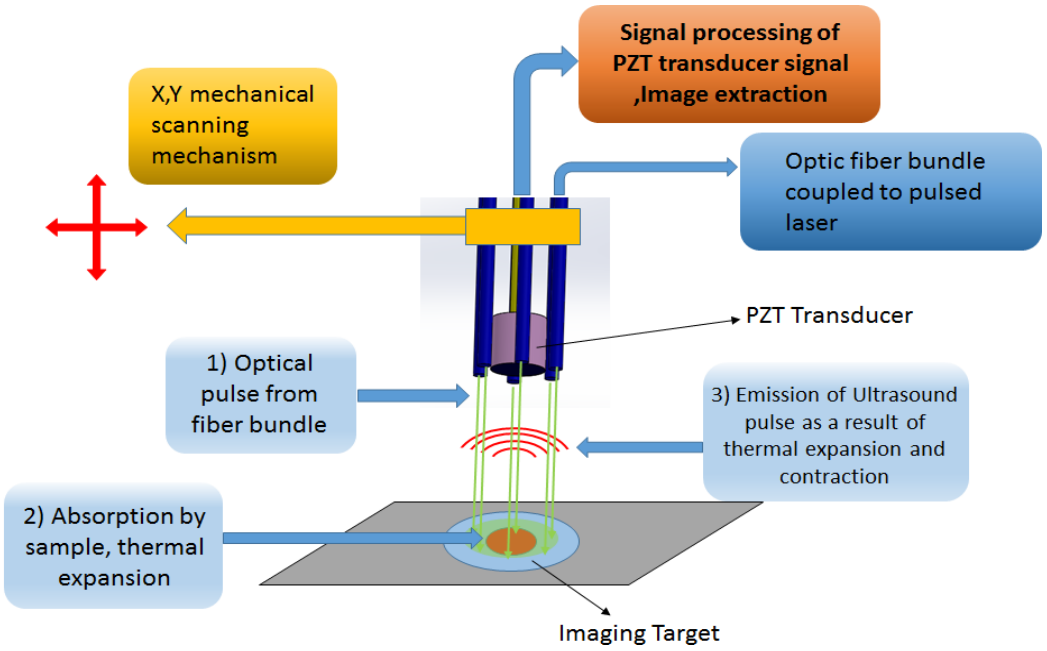

Figure 5.1. Principle behind PAI and the system used here. The optic fibers deliver the optical energy to the target to be imaged while being flexible enough to be mechanically scanned in a B-scan/ circular pattern.

In PAI, the target (e.g. tissue) to be imaged is illuminated with a short (nanosecond) pulse of light from a laser which creates a highly localized area of heating in the target. This heating subsequently causes a rapid pressure rise due to thermo-elastic

expansion, which in turn propagates as an ultrasonic acoustic wave referred to as a photoacoustic wave. This photoacoustic wave is then detected by an ultrasound transducer which is subsequently processed to reconstruct an image of the sample. Figure 5.1 gives an overview of the proposed PAI system utilizing optical fibers for light delivery. To generate a strong PA signal from the target, the ultrasound receiver must be as directly above the region on the target receiving the light pulse as possible.

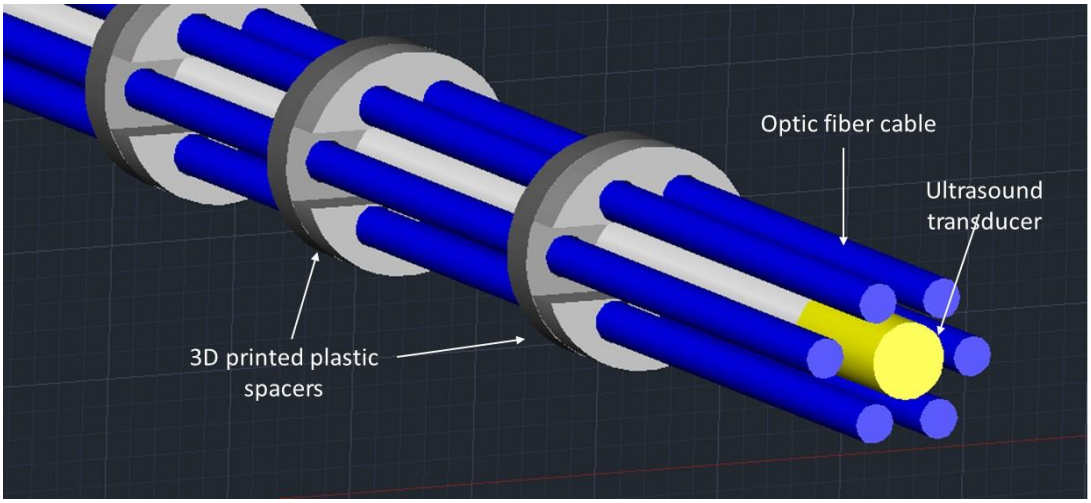

Figure 5.2. Photoacoustic imaging probe / cable assembly concept.

The previous setup in section 2.3.1 is most suitable only for imaging using pulse-echo. i.e, imaging using purely ultrasound transmission and receive echo from the target. This setup is not optimized to scan an optical fiber to enable photoacoustic imaging. To overcome this limitation, it is proposed here to construct a PA imaging probe that incorporates an ultrasound transducer as well as optical fibers for light delivery. As shown

in figure 5.2, the PA imaging probe is made up of 6 optic fiber cables whose core diameter is 400µm arranged in a hexagonal pattern around a single coaxial cable that connects to a commercially available PZT ultrasound transducer. The entire cable assembly is held together by spacers printed on a high resolution 3D printer in plastic.

Solidworks mechanical simulations were run to determine that 6 cables arranged in a hexagonal pattern were the smallest number of cables that would provide equal stiffness in all directions when the whole assembly is subjected to bending. Figure 5.3 shows the mechanical bending simulation results carried out on such a configuration of cables.

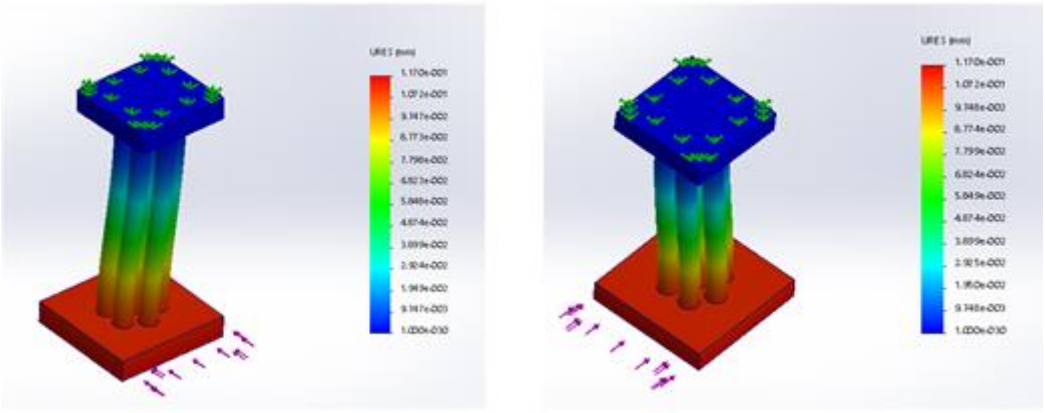

Figure 5.3. Solidworks simulation results for bending of 6 identical cables arranged in a hexagonal pattern (in addition to one center cable). X and Y axis forces resulted in the same deviation showing that the mechanical stiffness is identical in all directions in this configuration.

The square block on the bottom is subjected to force separately in the X and Y directions and the deflection is found to be the same in both cases. It is important for the

probe to have equal stiffness in all directions if it is going to be scanned in a circular/spiral pattern for 3D imaging. Unequal stiffness will result in a non-circular scan pattern and will make image reconstruction difficult.

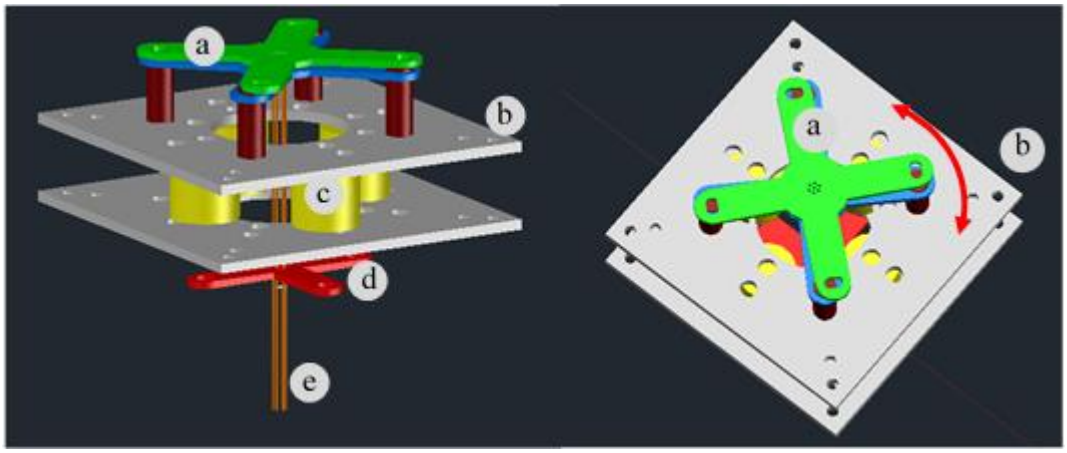

Figure 5.4. CAD drawing showing overall structure of PA probe scanning mechanism. a) Cable locking mechanism b) Magnetic coil holder plates c) Magnetic coils d) Magnet holder for probe bending actuation e)PA imaging head- Ultrasound transducer + polished optic fiber.

Figure 5.4 shows the overall proposed system for the scanning mechanism with optical light delivery capability for PA imaging. As before, four coils are held vertically between two acrylic laser cut sheets. The PA imaging probe is suspended through this structure and anchored at a point above the coils by a locking mechanism that has the capability to twist and be tightened to hold all the cables secure while providing nearly equal force in all directions. Finally, a cross shaped permanent magnet holder attaches to the cable assembly which enables the transfer of force from the coils to bend the cable along the desired axis.

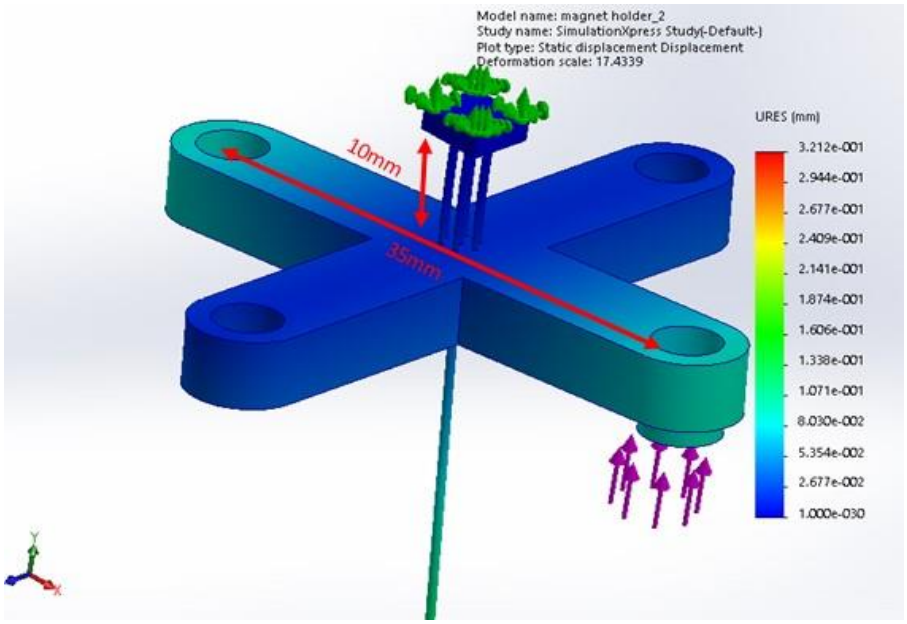

Figure 5.5. Simulation carried out on cable structure with7 Silicon cables arranged in a hexagonal pattern. A 1 Newton force at one of the ends of the magnet holder arms (shown with blue arrows) produced only 0.3mm deflection.

When simulations were initially run on solid works for the bending of the 7 cable assembly with a 1 Newton force, it was found that the deflection in the cable was extremely small and is shown in figure 5.5.The reason for such a small deflection is possibly due to the ideal nature of anchor points for all the cables (shown in green arrows in figure 5.5) in the simulation. In reality, this anchor point is made up of a spacer with holes where the cables are able to slide through. The assumption is that there is enough friction for the cables to slightly slide in and out of the anchor holes as the whole cable assembly bends. If this did not happen, it would be impossible for the cables to bend to any significant degree. To simplify the simulation, it was decided to replace the 6 cables

of diameter 400μm each and the coaxial cable in the center with one single cable to equivalent thickness which would theoretically offer a similar level of stiffness.

The force constant k of a cantilever beam fixed at one end and acted upon a force perpendicular to its length at the other end is given by [15]:

$$\boldsymbol{k = \frac{3EI}{L^3}} \qquad \textbf{Equation 5.1}$$

Where E= Elastic modulus of material, I = moment of inertia and L=length. The moment of inertia I is in turn given by [15]:

$$\textbf{I=}\boldsymbol{\frac{1}{12}m(3r^2 + L^2)} \qquad \textbf{Equation 5.2}$$

Where r= radius of the rod, L= Length and m=mass. From (5.1) and (5.2), we can see

$$\boldsymbol{k \propto \frac{(3r^2 + L^2)}{L^3}} \qquad \textbf{Equation 5.3}$$

Since the cable assembly consists of 6 optic fiber cables arranged circularly around a coaxial cable, as a simplification, it was assumed that we have 7 cables all bending together in parallel. This is equivalent to 7 springs connected together in parallel. In this configuration, the spring constants are added together to get the equivalent k for the entire system. If all 7 cables are to be replaced by one equivalent cable of larger diameter and same length. In equation 5.3 given that length L is a constant. The stiffness k is only dependent on r. If k' denotes the new equivalent stiffness of this setup with a corresponding radius r'

$$\boldsymbol{k' = 7 \times k} \qquad \textbf{Equation 5.4}$$

Which gives from 5.3:

$$r'^2 = 7 \times r^2 \qquad \textbf{Equation 5.5}$$

$$\textbf{Or,} \quad r' = \sqrt{7} \times r \qquad \textbf{Equation 5.6}$$

If r= 400 μm, then, r' becomes 1.058 mm, which is the basis for the simulation in section 2.2 shown in figure 2.4, which yields a 10mm deflection with a 1N force acting on a silicon rod of 30mm length, which was the starting point for the entire design process. Since the PZT transducer used for ultrasound detection and pulse transmission used here comes pre-fabricated with a BNC connector at the other end, it was not possible to create a spacer with a hole diameter large enough to hold only the cable and then push it through like the optic fibers. A novel interlocking mechanism was designed to accommodate both the fibers and the coaxial cable into a tightly bound single cable so that it can be scanned mechanically as a single entity.

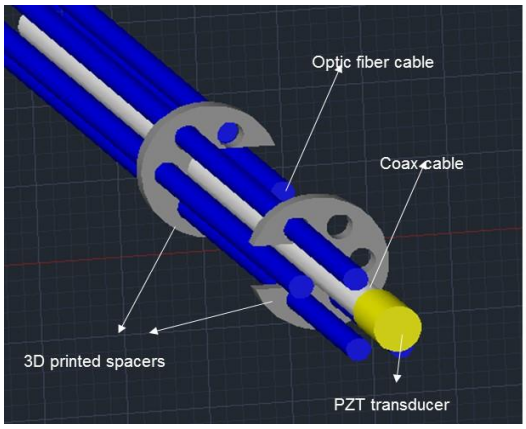

Figure 5.6. PA probe assembly process. The PZT transducer cable could not be pushed through the small holes like it was done for the optic fiber cables (blue) , so a novel interlocking mechanism had to be devised to enable the incorporation of the fibers and the coaxial cable

Figure 5.7. 3D printed Spacers (left) and assembled PA probe (right).

5.2 Photoacoustic testing

To test the PA imaging capability of this probe, it was fixed vertically onto a stand and the target was scanned on an x,y scanning stage. The fibers were coupled into a pulsed laser and LabView stepped the x,y stage in a zigzag pattern over a target and also acquired data from the PZT transducer from an oscilloscope. Matlab was then used to create a surface plot of the raw data acquired. The setup is shown in figure 5.8. Figure 5.9 shows the target used for PA imaging. It consists of two black tape pieces 5mm x5mm stuck on 2 platforms separated by a height of ~10mm. Figure 5.10 shows the pulse received by the transducer in the PA probe at a distance of approximately 20mm from the target. Depth information is gleaned from the time taken for US pulse to travel to the transducer once the laser hits the target. Figure 5.11 shows a surface plot of the raw data collected from the oscilloscope once the PA probe has traversed across the entire target

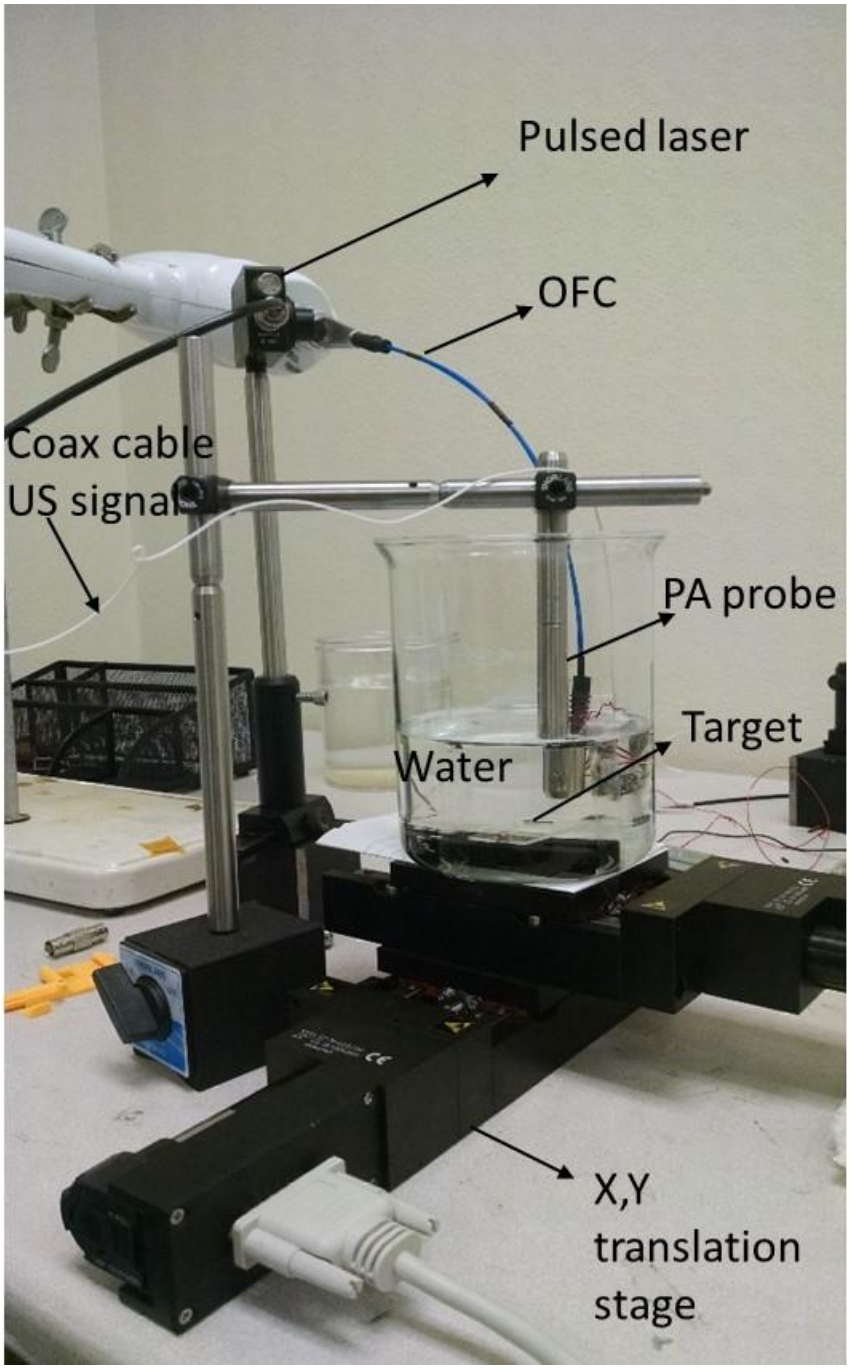

Figure 5.8. Setup used to test the PA imaging probe.

Figure 5.9. Imaging target for Photoacoustic imaging.

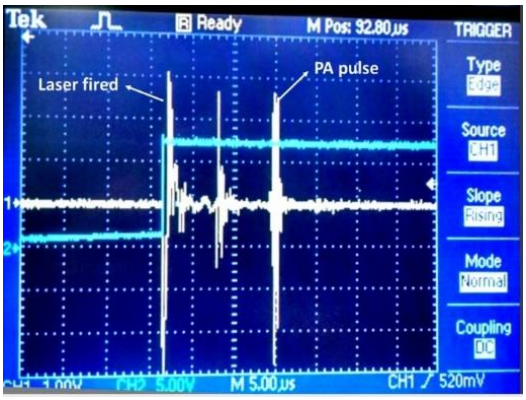

Figure 5.10. Oscilloscope screenshot showing PA pulse received by the ultrasound transducer after the laser has fired and struck the target. At a distance of more than 2cm. Depth information is gleaned from the time taken for US pulse to travel to the transducer once the laser hits the target.

It can be clearly seen that the gathered data matches closely with the actual target shown in figure 5.10. The purpose of this experiment was to demonstrate that this probe is capable of generating a PA image and it was successfully accomplished

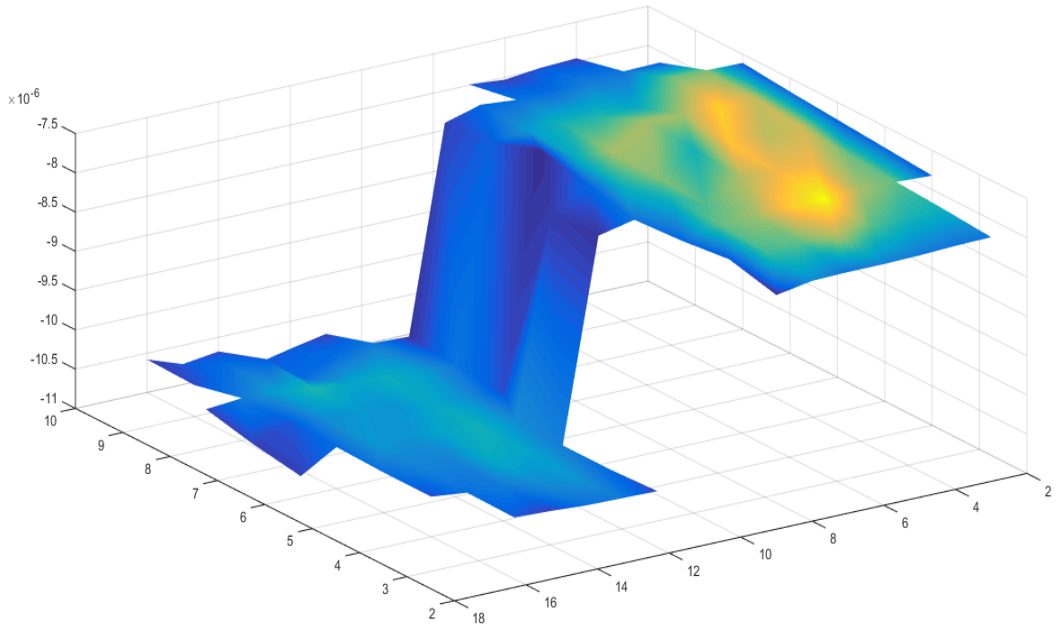

Figure 5.11. PA pulse data of target shown in figure 2.24. Z axis is time of occurance of the PA pulse (indirectly the depth, since it can be calculated given speed of sound in water.) X and Y is distance. The color represents amplitude of PA signal voltage.

5.3 Photoacoustic probe scanning

In addition to building a scanning US probe as shown in figure 3.9, the PA probe described here so far was also assembled into the scanning mechanism in the configuration shown in the CAD illustration in figure 5.4 initially. However, the mechanical bending of the probe was found to be inadequate since there was torsion in the cable as explained in section 2.3 .This initial prototype is shown in figure 5.12. Using the gimbal mechanism in figure 2.13, where the gimbal hinges provide no stiffness of their own, the scanning probe assembly was rebuilt with the PA probe.

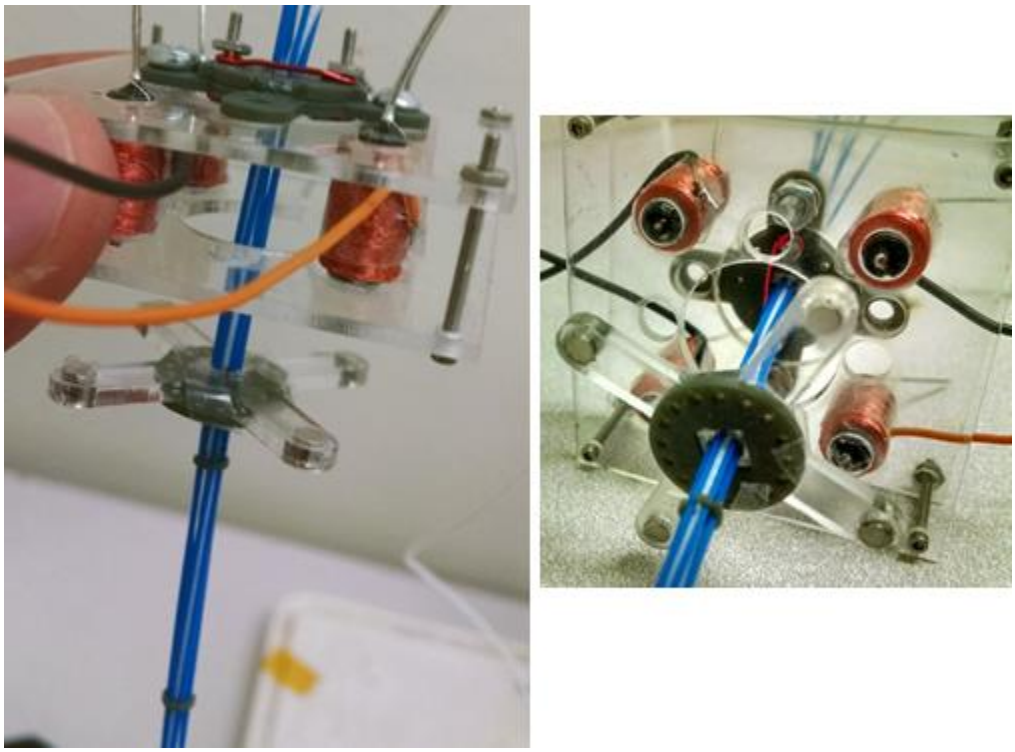

Figure 5.12. Initial prototype of scanning probe without the gimbal mechanism which resulted in torsion of the PA probe and very little deflection.

The overall stiffness of the PA probe however, proved to be too high for the magnet and coil mechanism to generate enough force and achieve a deflection of 30mm. The maximum deflection obtained from the second prototype with the gimbal mechanism was a ~15mm diameter circular scanning pattern, which is not adequate for good coverage of the target. The PA probe assembled into the gimbal mechanism is shown in figure 5.13. This setup relies on the stiffness of the probe assembly which consists of the optic fiber cables as well as the coaxial US transducer cable to provide the restoring force to bring back the probe to its zero position.

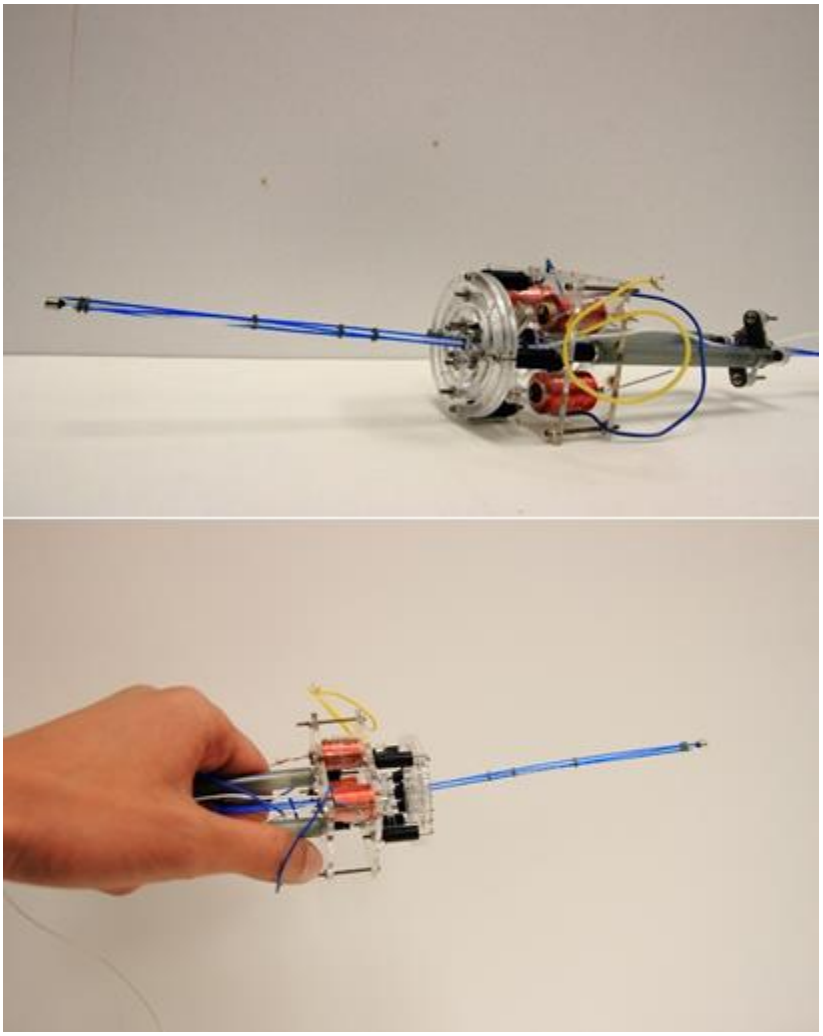

Figure 5.13. PA probe incorporated with the gimbal scanning mechanism.

An issue noted while testing this setup was that the bending of the cable was not repeatable in all directions, causing an instability in the scanning pattern. The reason for this behavior is due to slight variation in the hole sizes for the 3D printed plastic spacers (figure 5.7). Some holes were slightly larger than the optic fiber cable diameter, which did

not offer much frictional resistance while other holes were smaller and offered so much resistance that the cable had to be pulled through with considerable application of force using pliers during the assembly process.

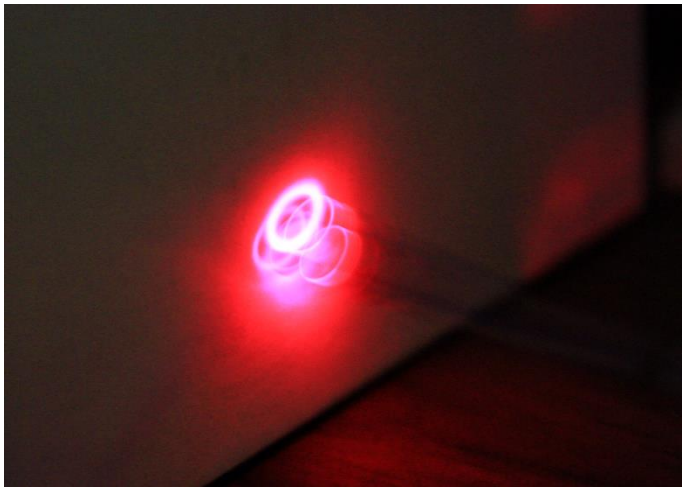

Figure 5.14. Scanning pattern generated by the photoacoustic imaging probe being scanned in a circular pattern taken with a 3 second exposure photograph. The scanning diameter was limited to about 15mm and the uneven cable stiffnes resulted in insatbility. The multiple rings are due to light emerging out of each optic fiber cable.

This uneven frictional force acting on the PA probe assembly as it bends to form a circular scanning pattern increases the apparent stiffness of the cable assembly (as seen in the ideal situation in the simulation shown in figure 5.5) or at times provided un-repeatable scanning patterns as the cables slid and grabbed the plastic spacer holes randomly. The scan pattern produced is shown in the long exposure photograph in figure 5.14. A possible remedy for this issue was to create spacers by etching silicon to improve precision, but was not explored in this research and is one of the future improvements that

can be done to improve performance.

Due to these complications with the unreliable scanning of the photoacoustic probe, for the purpose of this research, it was decided that the scanning mechanism would be limited to pulse echo ultrasound detection only. Section 3.2 went into the details of the mechanical scanning characterization of the US only probe.

6. SUMMARY AND FUTURE WORK

In this research, a low cost scanning mechanism that enables the scanning of a single element transducer for ultrasound imaging was developed. It is capable of generating either B-scan patterns at several different angles or circular/ spiral patterns by varying the phase and amplitude of the driving coils. This capability makes this scanning probe software programmable to enable scanning a variety of shapes. Pulse echo ultrasound imaging was carried out in B-scan mode at multiple angles on a 0.9 mm pencil lead. The same design was further shown to be expandable to photoacoustic imaging by incorporating optic fiber cables into the imaging probe. While this particular prototype was unable to fully scan the ultrasound transducer in a perfectly circular path due to mechanical limitations, the prototypes developed as part of this research can be used as a platform for further refinement of the design.

Several improvements can be made to enhance the accuracy and robustness of the scanning mechanism, mainly by improving the materials used in the construction such as laser cut acrylic and 3D printed plastic which has a relatively large error in the dimensions produced.

Another aspect of the design that can be improved is to make the whole scanning system closed loop by using PID control. A position error sensor can be easily incorporated into the magnet holder arm of the scanning mechanism using a magnetic or capacitive transducer that converts the angle position of the magnet holder into a corresponding analog error voltage value.

Incorporating probe position information will also help simplify and increase the robustness of the image reconstruction algorithms, since image formation requires both the actual ultrasound data as well as position information to successfully reconstruct a 3D image of the target. Having the exact relative positon information will allow the scanning probe to be scanned in any arbitrary shape and still generate coherent images. This is very useful especially when the imaging probe is going to be hand held and used for in-vivo imaging, where hand holding the probe will introduce mechanical shock and vibrations which will alter the shape of the scanning pattern.

A commercially viable design will need to be completely immersed in water to make it truly hand hold-able. In such a case, the transducer needs to be placed in water to to match the acoustic impedance of the target to the transducer. This can be achieved by using something as simple as a plastic PVC tube or equivalent material to house the entire scanning mechanism and fill it with water. Doing this will change the mechanical characteristics of the scanning mechanism due to the damping of the fluid and the coils will also need to be waterproofed by coating the electronics in an insulating material. Since the magnetic permeability of water is very close to that of air, the magnetic force generated will be almost the same but the deflection of the probe and the resonant frequency will be significantly lower due to resistance provided by the surrounding water. Furthermore, the coils used in the setup are capable of being driven at higher voltages than what was used in this study, which will significantly increase the generated driving force.

REFERENCES

[1] S. N. Narouze, “Basics of Ultrasound Imaging,” in Atlas of ultrasound-guided procedures in interventional pain management, New York: Springer, 2011, pp. 13–15.

[2] “A,B and C scan displays,” Classle.net, Apr-2009. [Online]. Available at: https://www.classle.net/book/ab-and-c-scan-displays. [Accessed: May-2015].

[3] C. Frazier and W. O'brien, “Synthetic aperture techniques with a virtual source element,” IEEE Transactions on Ultrasonics, Ferroelectrics and Frequency Control., vol. 45, no. 1, pp. 196–207, 1998.

[4] J. A. Jensen, S. I. Nikolov, K. L. Gammelmark, and M. H. Pedersen, “Synthetic aperture ultrasound imaging,” Ultrasonics, vol. 44, no. 1, pp. E5–15, 2006.

[5] J. Woo, “A short History of the Real-time ultrasound scanner,” Obstetric ultrasound -- a comprehensive guide to ultrasound scans in pregnancy, 1998. [Online]. Available at: http://www.ob-ultrasound.net/history-realtime.html. [Accessed: May-2015].

[6] T. R. Nelson and D. H. Pretorius, “Three-dimensional ultrasound imaging,” Ultrasound in Medicine & Biology, vol. 24, no. 9, pp. 1243–1270, 1998.

[7] D. Turnbull and F. Foster, “Fabrication and characterization of transducer elements in two-dimensional arrays for medical ultrasound imaging,” IEEE Transactions on Ultrasonics, Ferroelectrics and Frequency Control IEEE Trans. Ultrason., Ferroelect., Freq. Contr., vol. 39, no. 4, pp. 464–475, 1992.

[8] G. Lockwood, J. Talman, and S. Brunke, “Real-time 3-D ultrasound imaging using sparse synthetic aperture beamforming,” IEEE Transactions on Ultrasonics, Ferroelectrics and Frequency Control IEEE Trans. Ultrason., Ferroelect., Freq. Contr., vol. 45, no. 4, pp. 980–988, 1998.

[9] Reinstein, D. Z., Silverman, R. H., Raevsky, T., Simoni, G. J., Lloyd, H. O., Najafi, D. J., & Coleman, D. J. , “Arc-scanning very high-frequency digital ultrasound for 3D pachymetric mapping of the corneal epithelium and stroma in laser in situ keratomileusis”, Journal of Refractive Surgery, vol. 16, no. 4, pp. 414-430, 2000

[10] Z. Song, “Three-Dimensional Ultrasound Imaging,” in Handbook of 3D machine vision optical metrology and imaging, Boca Raton: CRC Press, Taylor & Francis Group, 2013, p. 304.

[11] A. Fenster and D. Downey, “3-D ultrasound imaging: a review,” IEEE Eng. Med. Biol. Mag. IEEE Engineering in Medicine and Biology Magazine, vol. 15, no. 6, pp. 41–51, 1996.

[12] Q. Huang, Y. Zheng, M. Lu, and Z. Chi, “Development of a portable 3D ultrasound imaging system for musculoskeletal tissues,” Ultrasonics, vol. 43, no. 3, pp. 153–163, 2003.

[13] A. Fenster, K. Surry, W. Smith, J. Gill, and D. B. Downey, “3D ultrasound imaging: applications in image-guided therapy and biopsy,” Computers & Graphics, vol. 26, no. 4, pp. 557–568, 2002.

[14] R. Clarke, “The force produced by a magnetic field,” Coils, 2010. [Online]. Available at: http://info.ee.surrey.ac.uk/workshop/advice/coils/force.html. [Accessed: May-2015].

[15] R. J. Roark and W. C. Young, “Beams: Flexure of Straight Bars,” in Roark's formulas for stress and strain, 7th ed., New York: McGraw-Hill, 2002, p. 199.

[16] “D22-N52 Specification Sheet,” Product Performance Specifications, 2015. [Online]. Available at: https://www.kjmagnetics.com/specification.sheet.php. [Accessed: May-2015].

[17] R. Nave, “Increasing Current in Coil,” Inductance of a coil of wire, 2012. [Online]. Available at: http://hyperphysics.phy-astr.gsu.edu/hbase/magnetic/indcur.html. [Accessed: May-2015].

[18] H. Wheeler, “Formulas for the Skin Effect,” Proceedings of the IRE, vol. 30, no. 9, pp. 412–424, 1942.

[19] H. Wheeler, "Simple Inductance Formulas for Radio Coils," Proceedings of the I.R.E., vol. 30, no. 9, pp. 1398-1400, 1928.

[20] I. R. Sinclair and J. Dunton, “Inductive and Tuned Circuit Components,” in Practical electronics handbook, 6th ed., Amsterdam: Elsevier/Newnes, 2007, p. 66.

[21] “Part number 70F501AF-RC,” Varnished Chokes, 2003. [Online]. Available at: http://www.bourns.com/data/global/pdfs/70f_series.pdf. [Accessed: May-2015].

[22] T. Stepinski and F. Lingvall , "Synthetic aperture focusing techniques for ultrasonic imaging of solid objects," Synthetic Aperture Radar (EUSAR), 2010 8th European Conference on , vol., no., pp.1,4, 7-10 , 2010

[23] M. Xu and L. V. Wang, “Photoacoustic imaging in biomedicine,” Rev. Sci. Instrum. Review of Scientific Instruments, vol. 77, no. 4, pp. 041101–041101, 2006.

[24] H. F. Zhang, K. Maslov, G. Stoica, and L. V. Wang, “Functional photoacoustic microscopy for high-resolution and noninvasive in vivo imaging,” Nat Biotechnol Nature Biotechnology, vol. 24, no. 7, pp. 848–851, 2006.